Gondwana Research 146 (2025) 93–106

Contents lists available at ScienceDirect

Gondwana Research

journal homepage: www.elsevier.com/locate/gr

Divergent subduction of a tearing slab controls deep carbon recycling efficiency: Helium and carbon isotopic evidence from the southeast Tibetan Plateau

Yingchun Wang [a,b,c], Xiaocheng Zhou [d,*], Jiao Tian [d], Pengfei Chen [a,b], Miao He [d], Yucong Yan [d], Bingyu Yao [e], Zhongping Li [f], Chunhui Cao [f], Hikaru Iwamori [c]

[a] State Key Laboratory of Oil and Gas Reservoir Geology and Exploitation, Chengdu University of Technology, Chengdu 610059, China
[b] College of Energy (College of Modern Shale Gas Industry), Chengdu University of Technology, Chengdu 610059, China
[c] Earthquake Research Institute, The University of Tokyo, Tokyo 113-0032, Japan
[d] United Laboratory of High-Pressure Physics and Earthquake Science, Institute of Earthquake Forecasting, China Earthquake Administration, Beijing 100036, China
[e] School of Earth Sciences and Resources, China University of Geosciences, Beijing 100083, China
[f] Northwest Institute of Eco-Environment and Resources, Chinese Academy of Sciences, Lanzhou 730000, China

ARTICLE INFO

Handling Editor: T. Gerya

Keywords:
Hot spring degassing
He–CO_2 systemics
Slab tearing
Carbon recycling efficiency
Southeast Tibetan Plateau

ABSTRACT

Variations of helium isotopic compositions across tectonic belts and at regional scales provide critical insights into crust–mantle interactions and the transport of heat and volatiles from the Earth's interior. In this study, we report geochemical data from 26 thermal springs, including 51 newly analyzed samples, and integrate a broader dataset comprising 854 samples from 350 sites distributed along the Xianshuihe and Red River fault zones of southeastern Tibetan Plateau. Distinct helium isotopic anomalies and heterogeneous contributions of recycled carbon sourced from altered oceanic crust (AOC) were identified using combined analyses of $^3He/^4He$ ratios and $\delta^{13}C$–CO_2 signatures, supported by an updated helium–carbon coupling model. Clear spatial contrasts were observed across the helium boundary zone (HBZ), with $\delta^{13}C$–CO_2 and $CO_2/^3He$ ratios revealing marked differences between the northwestern and southeastern sectors. The mantle-derived helium-3 flux reaches approximately 1.7×10^4 atoms m^{-2} s^{-1} in the northwest, compared with 1.04×10^4 atoms m^{-2} s^{-1} in the southeast. These disparities align closely with geophysical evidence indicating the presence of a slab tear in the Indian lithosphere beneath the Lijiang–Xiaojinhe fault (LXF). In addition, a decarbonation boundary linked to slab subduction was delineated near 26°N with higher recycled carbon fluxes in the northwest (~35 %) than those in the southeast (~22 %). This asymmetry is attributed to variations of subduction depth and angle associated with tearing of the Indian slab. The results of this study highlight the pivotal role of slab tearing and divergent subduction processes in modulating the efficiency and spatial heterogeneity of deep carbon recycling along convergent plate margins.

1. Introduction

Sediments and volatiles associated with subducting slabs are transported into the Earth's interior through subduction zones, potentially reaching the mantle and being recycled to the atmosphere, as Earth degassing mainly occurs with volcanic activity and regions of active faults (Pinti et al., 2011; Plank and Manning, 2019; Zhao et al., 2022). This volatile cycle is a crucial part of the Earth's material exchange and significantly influences its climate and habitability (Li et al., 2023a; Lopez et al., 2023; Nakao et al., 2016; Zuo et al., 2024). The tectonic zone provides conditions for releasing deep-seated volatiles (such as carbon and helium), especially in different tectonic settings such as arc–continent collision zones, rift zones, continent–continent collision zones, and subduction zones, which are key pathways for volatile transfer (Umeda et al., 2012; Hiett et al., 2021; Caracausi et al., 2022; Li et al., 2022). Early Earth subduction at higher temperatures (hot subduction) transferred negligible volatiles to the deep Earth, whereas modern subduction at lower temperatures (cold subduction) causes significant volatile transport, affecting the efficiency of volatile recycling over geological time (Hanyu et al., 2019; Li et al., 2020a; Randazzo

* Corresponding author.
E-mail address: zhouxiaocheng188@163.com (X. Zhou).

https://doi.org/10.1016/j.gr.2025.06.001
Received 30 January 2025; Received in revised form 8 June 2025; Accepted 10 June 2025
Available online 13 June 2025

et al., 2021; Zhang et al., 2024). Some studies suggest that most subducted carbonates undergo decarbonation and dissolution in the mantle wedge and enter the recycling process at relatively shallow depths (Kelemen and Manning, 2015; Foley and Fischer, 2017), whereas others indicate that subducted carbonates may penetrate deeper into the mantle transition zone (Thomson et al., 2016; Mazza et al., 2019). The depth at which decarbonation occurs is influenced by the characteristics of the subducting slab, which further contributes to the orders-of-magnitude differences observed in carbon cycling efficiency (Clift, 2017; Guo et al., 2017; Lages et al., 2021; Tian et al., 2019). The amount of carbon delivered to the deep Earth by modern subducting slabs varies significantly, owing to differences in slab formation, evolution, and sedimentary history (Asaah et al., 2015; Plank and Manning, 2019; Tian et al., 2023; Zummo et al., 2024). This variability may also account for large uncertainties in the estimates of modern subduction-related carbon recycling efficiencies. However, the influence of different slab morphologies on carbon recycling efficiency remains unconstrained.

Volatiles in Earth's interior are released into the atmosphere mainly via volcanoes and fault systems (Caracausi and Sulli, 2019; Hao et al., 2024). Conversely, the release and evolution of volatiles, such as helium, are powerful tracers of regional tectonics and are sensitive to crust–mantle interactions and other processes within the crust (Gilfillan et al., 2019; Hao et al., 2020; McCrory et al., 2016). Helium isotopes ($^3He/^4He$), as an inert volatile, are widely used to trace volatile sources and tectonic activity owing to their distinct end-members in the crust (0.02 R_A, where R_A is $^3He/^4He$ of air $= 1.39 \times 10^{-6}$), atmosphere (1 R_A), and mantle (subcontinental lithospheric mantle, 6.1 ± 0.9 R_A) (Graham, 2002; Day et al., 2015). The transport of mantle helium to the surface is accompanied by carbon dioxide as a carrier gas; therefore, the coupling of helium and carbon has been widely used to trace the release of volatiles (Correale et al., 2015; Wang et al., 2024; Hao et al., 2025). Active volcanic regions, mid-ocean ridges, and plate boundaries are all concentrated areas of carbon release from the Earth's interior. Moreover, convergent plate boundaries play a vital role in the carbon cycle as they influence Cenozoic climate change, especially in the Alpine–Himalayan orogenic belt (Zhao et al., 2022). Identifying the proportion and migration of deep carbon is crucial for understanding the relationship between tectonics and climate.

Decarbonation from volcanic and fault-related rocks is influenced by subduction and primarily originates from the subducting slab, mantle wedge, and overlying crust (Li et al., 2019; Lopez et al., 2023). Subducting slabs transport materials from trench sediments, marine carbonates, and altered oceanic crust (AOC) into the mantle, resulting in distinct carbon isotopes as AOC contains inorganic carbonate with $\delta^{13}C$ of approximately 0.8 ‰ ± 0.5 ‰, while mantle-derived carbon isotopes show $\delta^{13}C$ values of around −6.5 ± 2 ‰ (Hilton et al., 2002; Sano and Fischer, 2013). Sediments of subducting slabs and the overlying crust have variable carbon isotopes due to isotopically heavy carbonates (~0 ‰) and isotopically light sedimentary organic matter (SOM; ~ −30 ‰) (Van Soest et al., 1998; Barry et al., 2013). As a reactive gas, carbon dioxide undergoes secondary processes in hydrothermal systems such as dissolution, degassing, and precipitation, altering end-member information and adding complexity to carbon evolution (Rizzo et al., 2015; Wang et al., 2023).

In this study, we investigated the influence of lithospheric slab morphology, particularly slab tearing, on the efficiency of deep carbon recycling at the convergent margin of the southeastern Tibetan Plateau. By analyzing and compiling $^3He/^4He$ and $\delta^{13}C$–CO_2 isotopic data from 376 sites (905 samples, including 26 newly sampled thermal springs with 51 samples) on the southeastern Tibetan Plateau, we assessed spatial variations in mantle-derived volatile fluxes across major tectonic blocks. Specifically, based on an improved helium–carbon coupling model, we identified a two-stage deep carbon release process and identified obvious helium isotope and AOC ratio differences on the north and south sides of the Lijiang–Xiaojinhe Fault (LXF). By integrating these observations with the seismic tomography results, we identified a slab-tearing zone near the LXF, and evaluated its role in controlling deep carbon release pathways and volatile partitioning. This research provides significant insights into deep element cycling in collisional boundary regions, the uplift process of the Tibetan Plateau, and Earth's habitability.

2. Geological settings of the study area

The southeastern Tibetan Plateau experienced significant Cenozoic tectonic activity related to the Plateau interior. During the mid-Miocene, material from the Plateau extruded southeastward (Liu et al., 2014; Zhang et al., 2022). Tectonic activity increased at ~20 Ma, with clockwise rotation beginning at approximately 15 Ma (Li et al., 2020b). Fault systems near the LXF show notable differences between the northern and southern sides (Fig. 1). The north of the thrust fault system lies in high-altitude terrain with a thick crust (approximately 65 km) and high heat flow (90 mW/m^2) (Dong et al., 2016). In contrast, the southern side has low-altitude terrain with a thin crust (approximately 35 km) and low heat flow (65 mW/m^2) (Liu et al., 2024).

The southeastern Tibetan Plateau is a highland area characterized by significant crustal strain, active faults, and seismicity (Royden et al., 2008; He et al., 2021). It includes three major tectonic blocks: the Songpan–Ganzi (SGB), Yangtze, and Indochina blocks, which interact along major faults, including the strike-slip Red River (RRF), Xianshuihe (XSHF), and Xiaojiang (XJF) faults, and thrust faults like the Longmenshan (LMSF) and Lijiang–Xiaojinhe (LXF) thrust belts (Tapponnier et al., 2001; Bai et al., 2010). These fault systems divide the southeastern Tibetan Plateau into the Dianzhong block (DZB), Tengchong–Baoshan block (TCB), and Sichuan Basin (SCB) (Zhang, 2013). Permian basalts from the Emeishan large igneous province are widespread in the southwest of the Yangtze Block, forming arcuate belts, with the inner belt as the stable core of the DZB (Li et al., 2020b). The XJF within the Yangtze Craton has been reactivated owing to Plateau expansion, showing significant slip and frequent earthquakes (Zhang, 2013).

3. Materials and methods

3.1. Sampling and measurements

Gas samples from 26 hot springs in the TCV, TCB, and TPSE were collected over 5 years and analyzed for helium and carbon isotopes (Fig. 1, Table S1). Gas samples were collected using the gas drainage method (Hilton et al., 2002), immersing an inverted funnel with a silicone tube into the mouth of the hot spring, rinsing the entire pipe thoroughly with hot water for 30 min, inserting the outlet of the pipe into a 50 mL lead glass bottle filled with hot spring water, and then sealing with a silicone plug when the water in the bottle remained at approximately 1/3. Analyses were performed within 1 month of sampling. Among them, 7 samples from the south of LXF, 4 from the intersection of XJF and RRF, and 21 from around the Eastern Himalayan Syntaxis (EHS) were newly collected, adding to the dataset differs that collected by Zhang et al. (2021) and providing an opportunity to elucidate crust–mantle interaction within the southeastern Tibetan Plateau. We compiled hot spring gas data within the southeastern Tibetan Plateau from the past 20 years (>50 literatures, Table S2) for spatial analysis of gas ratios (CO_2/N_2, N_2/Ar), helium isotopes, and carbon isotopes along the XSHF and RRF (for details, please see Text S1 and Text S2). The helium and carbon fluxes were calculated across the five blocks of the study area (Fig. 1).

3.2. Revised helium and carbon coupling model

From the perspective of carbon evolution and migration, mantle carbon, subducted slab carbon, and carbon within thick crust influence carbon sources in hot springs. Carbon can be divided into three

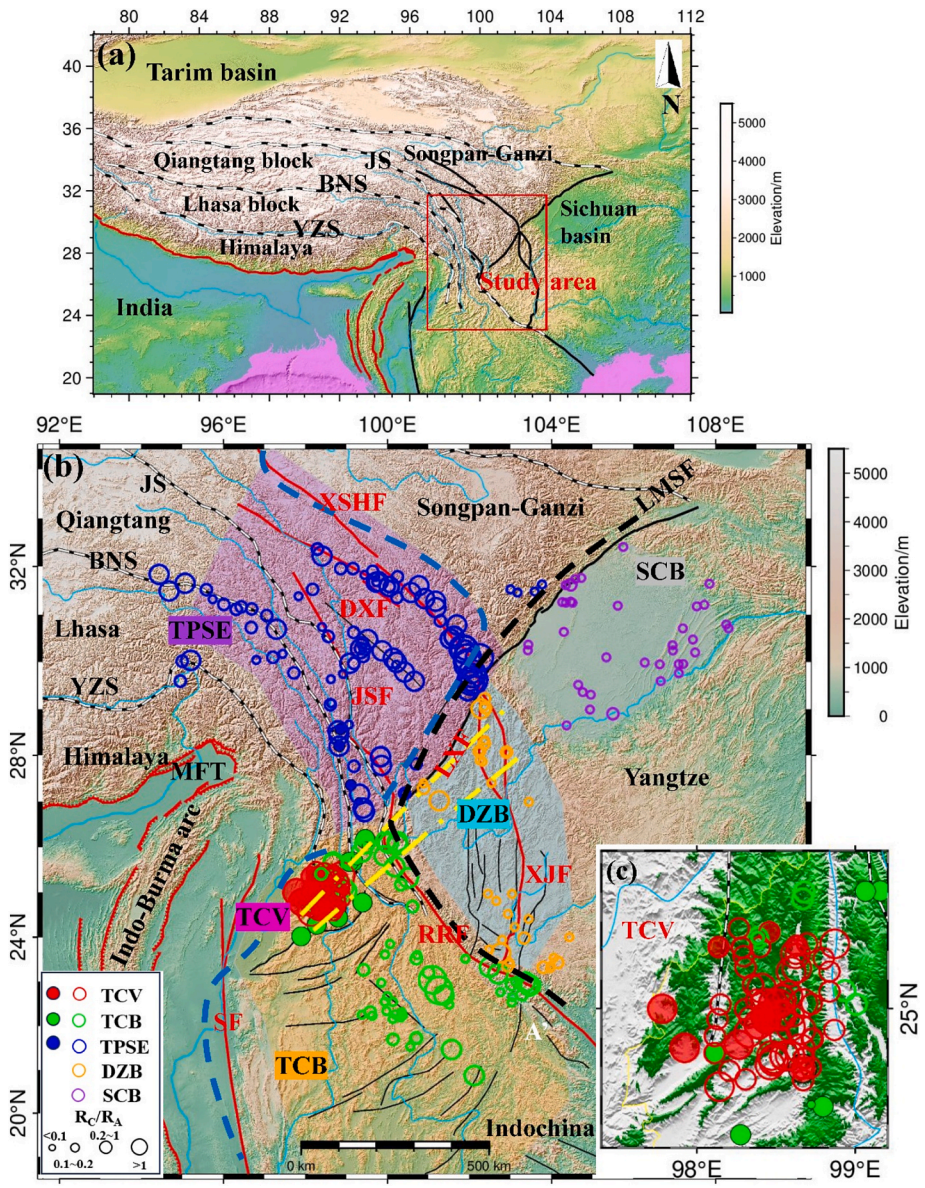

Fig. 1. (a) The tectonic setting of the Tibetan Plateau and division of tectonic blocks. (b) Sampling sites and distribution of helium isotopes from hot spring in the study area. (c) Enlarged view of sample sites of TCV. Helium isotopes are categorized into four sizes, with solid circles representing data from this study and open circles representing compiled data (Table S1 and Table S2). Shading denotes the five tectonic blocks (TPSE, DZB, TCB, TCV, and SCB) in the study area. Yellow dashed lines indicate the location of slab tearing observed in seismic tomography; blue and black dashed lines are the lithospheric frontiers of Indian mantle and Yangtze mantle, respectively (Hou et al., 2024). Abbreviations: JS: Jinshajiang Suture. BNS: Bangong–Nujiang Suture. YZS: Yarlung Zangbo Suture. MFT: Main Frontal Thrust. SF: Sagaing Fault. JSF: Jinshajiang Fault. XSHF: Xianshuihe Fault. DXF: Dege–Xiangcheng Fault. RRF: Red River Fault. XJF: Xiaojiang Fault. LMSF: Longmenshan Fault. LXF: Lijiang–Xiaojinhe Fault. TPSE: SE Tibetan Plateau. DZB: Dianzhong block. TCB: Tengchong–Baoshan block. TCV: Tengchong volcano. SCB: Sichuan Basin.

endmembers (Li et al., 2020a; Lopez et al., 2023): depleted MORB mantle (DMM), altered oceanic crust (AOC), and continental crust (CC) (Text S3). In this study, CC represented crustal carbon, including decarbonated carbonate rocks and organic sediments.

Subducted oceanic slab carbon, which is a recycled carbon endmember, is composed of carbonates and oceanic sediments from the oceanic lithosphere. Carbonate rocks from subducted slabs dominate the recycled carbon endmembers (>80 %; Clift, 2017; Zhao et al., 2025). Thus, this study focused on AOC carbon as the primary recycled carbon endmember, defined as:

$$\delta^{13}C_f = \frac{f_{DMM}\delta^{13}C_{DMM}C_{DMM} + f_{AOC}\delta^{13}C_{AOC}C_{AOC} + f_{CC}\delta^{13}C_{CC}C_{CC}}{f_{DMM}C_{DMM} + f_{AOC}C_{AOC} + f_{CC}C_{CC}} \quad (1)$$

$$R_{A,f} = \frac{f_{DMM}R_{A,DMM}He_{DMM} + f_{AOC}R_{A,AOC}He_{AOC} + f_{CC}R_{A,CC}He_{CC}}{f_{DMM}He_{DMM} + f_{AOC}He_{AOC} + f_{CC}He_{CC}} \quad (2)$$

$$f_{DMM} + f_{AOC} + f_{CC} = 1 \quad (3)$$

The mantle carbon endmember primarily considers DMM carbon, as determined through geophysical surveys (e.g., magnetotelluric and seismic observations) in eastern Tibet. The endmember values for DMM, AOC, and CC carbon in the helium–carbon coupling model are provided in Table S1 and Table S2. Detailed methodologies and results are provided in Text S1 and Text S2.

4. Results and discussion

4.1. Helium and carbon inventories and secondary hydrothermal processes

4.1.1. Helium characteristics

Considering that measured $^3He/^4He$ ratios (R_M) may be affected by air-derived helium during sampling or measurement, helium air contamination was corrected using the X-factor determined from the air-normalized $^4He/^{20}Ne$ ratios and Bussen coefficients of Ne and He. The air-corrected $^3He/^4He$ ratios (R_C) are listed in Table S1 and Table S2. The calculated $^4He/^{20}Ne$ values of the samples ranged from 0.33 to 2622.6, which is higher than that of air (0.32) and the ASW (0.25). However, some samples had $^4He/^{20}Ne$ values close to the ASW end-member (Fig. 2a), suggesting that air contamination or meteoric water effects cannot be ignored (yellow area in Fig. 2a); these samples are not included in further discussion. Based on the volume content of CO_2 and N_2, the samples were divided into two types: CO_2-type and N_2-type. However, there was no significant difference in the helium isotope ratio between the two types in the corresponding blocks, indicating that the source of the gas may be closely related to variation in the tectonic units.

Statistical diagrams of the helium isotope values (Fig. S1 and Fig. S2)

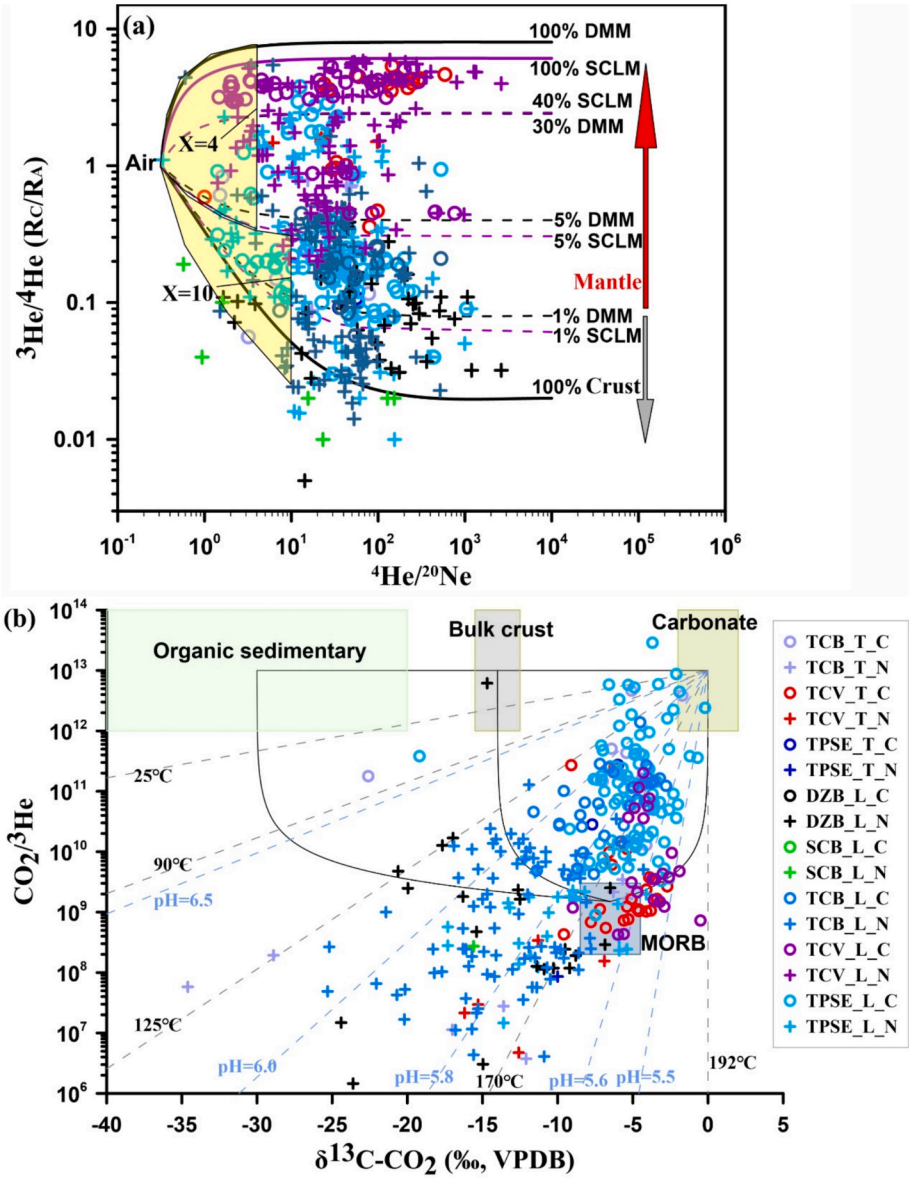

Fig. 2. (a) Helium–neon relationship for the five tectonic blocks. The plot is based on a three-endmember model (Sano and Marty, 1995), with crustal helium of $^3He/^4He = 0.02\ R_A$ and $^4He/^{20}Ne = 1000$, mantle helium (DMM, Graham, 2002) of $^3He/^4He = 8 \pm 1\ R_A$ (SCLM with $^3He/^4He = 6.1 \pm 0.9\ R_A$, Day et al., 2015) and $^4He/^{20}Ne = 1000$, and atmospheric helium of $^3He/^4He = 1\ R_A$ and $^4He/^{20}Ne = 0.318$ (Burnard et al., 1999). Yellow area denote X = 4 and X = 10 [$X = (^4He/^{20}Ne)_{measured}/(^4He/^{20}Ne)_{ASW}$], representing samples with significant air contamination (modified from Zhang et al., 2021). Percentages indicate crust–mantle mixing ratios. Helium in the DZB and SCB is predominantly crustal while that in the TPSE shows a wide range (1 % to 50 %) of mantle helium contributions. TCB exhibits a detectable ratio of mantle helium with a maximum value of 8 %. (b) $CO_2/^3He$ versus $\delta^{13}C$–CO_2 for hydrothermal gases, comparing carbon sources across the five blocks using the MORB, BC (Bulk crust), ORG (Organic Carbon), and CAR (Carbonate) endmembers. Black dashed lines represent carbon isotope fractionation models for calcite precipitation at temperatures of 25 °C, 90 °C, 125 °C, 170 °C, and 192 °C (Barry et al., 2020); blue dashed lines show the solubility relationships of gases in water at 50 °C with different pH values (Gilfillan et al., 2009). The model starts with metamorphic carbonate characterized by $\delta^{13}C$–CO_2 = 0.1 ‰ and $CO_2/^3He = 10^{13}$. Suffixes in the legend, T_C and L_C, denote CO_2-type gas from this study and the literature, respectively. T_N and L_N represent N_2-type gases for this study and the literature, respectively. Subsequent representation in related maps is the same.

showed that the TCV block has the highest values, whereas the TPSE and TCB have bimodal distributions with relatively high values. DZB and SCB exhibited low values, mostly < 0.1 R_A. According to the three end-member model, considering subcontinental lithospheric mantle (SCLM) at 6.1 ± 0.9 R_A and crustal values at 0.02 R_A, helium isotopes > 0.1 R_A indicate primary mantle degassing, while values < 0.1 R_A suggest a dominate crustal source (Ballentine and Burnard, 2002; Huang et al., 2024; Sano and Fischer, 2013). No significant correlation existed between the helium concentration and isotope values within these five blocks (Fig. S2), whereas helium-rich samples with lower isotope values suggest that crustal helium is predominate across most of the southeastern Tibetan Plateau. According to the tri-endmember diagram of helium–neon isotopes (Fig. 2a), helium is mainly controlled by uranium (U) and thorium (Th) enrichment in the crust (Zhang et al., 2021).

Mantle-derived helium varied across the five blocks (Fig. S3), with the TCV showing the most significant mantle contribution. The TCB and TPSE have mantle helium inputs, although not exceeding 9 %, whereas the DZB and SCB are dominated by crustal helium, with mantle contributions up to only 5 %. Statistical analysis of helium isotope ratios revealed a distinct separation between the TPSE and DZB, whereas the results linking the DZB and SCB indicate contiguous blocks with craton characteristics (Liu et al., 2024). Geophysical evidence supports this, with surface-wave tomography (Liu et al., 2021) and shear-wave splitting analysis (Li et al., 2023b) identifying high shear-wave velocity zones and regions of weak anisotropy beneath the DZB. These findings suggest the presence of a robust lithosphere beneath the DZB. Using dense array data from the eastern Tibetan Plateau to analyze the relative attenuation of teleseismic P-wave phases, Liu et al. (2024) found the presence of cratonic lithosphere beneath the DZB, comparable to that underlying the SCB. They further inferred that materials extruded eastward from the eastern Tibetan Plateau have traversed the LXF into the southwestern DZB within the lower crust, but were impeded at this boundary within the asthenosphere.

4.1.2. Carbon characteristics

The carbon inventory for five blocks in the southeastern Tibetan Plateau were estimated using a four-endmember carbon model (Fig. 2b), with DMM of $CO_2/^3He = 1.5 \times 10^9$ and $\delta^{13}C–CO_2 = -6.5$ ‰ ± 2.5 ‰, BC of $\delta^{13}C–CO_2 = -14$ ‰ ± 1.5 ‰, ORG of $\delta^{13}C\text{-}CO_2 = -30$ ‰ ± 10 ‰, and CAR of $\delta^{13}C\text{-}CO_2 = 0$ ‰ ± 2 ‰; the three crustal endmembers typically have higher $CO_2/^3He$ values, averaging of 10^{13} (Barry et al., 2020; Sano and Marty, 1995). The TCV, TPSE, and TCB exhibited higher mantle carbon signatures, whereas the DZB and SCB were dominated by crustal carbon sources (Table S1 and Table S2). The amount of CO_2 within the crust may be linked to regional metamorphism or mechanical-chemical processes generating CO_2 in collisional orogenic zones. Metamorphism primarily produces CO_2 through two mechanisms: (1) decarburization of calcium silicates at elevated temperatures and (2) dehydration reactions within the mineral phases. The heat that drives these metamorphic processes is predominantly attributed to progressive thermal conduction caused by plate fragment separation, plate rollback, or thermal relaxation associated with crustal thickening (Randazzo et al., 2021). This type of thermal metamorphism occurs not only in regions abundant in deeply metamorphosed rocks and limestones, but also in areas with limited carbonate rocks, where siliceous clastic metamorphic sediments (carbon contents < 2 %) are present (Lopez et al., 2023). Hot springs dominated by crustal carbon show significant metamorphic decarbonation within the crust from the Tibetan Plateau (Becker et al., 2008). According to the three-terminal diagram, BC is a carbon end-member of the crust, and the mixed zone of the three terminal elements is all CO_2-type gas, while N_2-type gas is outside the mixed zone. Owing to water–gas–rock interaction during gas migration, samples beyond the three-endmember limits (Fig. 2b) indicate CO_2 loss or He addition, which involves secondary processes such as calcite precipitation, gas dissolution differences, or high-helium fluid addition, as observed in geothermal systems, volcanic areas, and continental rift zones (Fig. 3; Ballentine and Burnard, 2002; Crossey et al., 2009; Hao et al., 2023). Therefore, our subsequent analysis focused on CO_2-type gases, as dissolution and precipitation processes can be dismissed.

We modeled the changes in He concentrations, $CO_2/^3He$, $CO_2/^4He$, and $N_2/^3He$ for CO_2 dissolution, calcite precipitation, and crustal He-rich fluid input. $CO_2/^3He$ decreased linearly with CO_2 loss as calcite precipitated, which is consistent with carbon isotope fractionation models (Fig. 3; Barry et al., 2020). N_2 and He enter the gas phase, as they are less soluble than CO_2, as the $CO_2/^4He$ and $N_2/^3He$ values change following the Rayleigh model. The decrease in $CO_2/^4He$ may have resulted from selective gas dissolution in the water. Calcite precipitation impacts $CO_2/^4He$ systematically as $\delta^{13}C$ varies, influenced by temperature and pH (Gilfillan et al., 2009). Precipitation occurs at around 150 °C, pH 6–8, and depths of 4–5 km based on a 3.5 °C/100 m gradient, which is a common depth for mountain groundwater circulation (Li et al., 2022; Somers and McKenzie, 2020; Wang et al., 2021, 2022).

A significant relationship among CO_2-type gases in the study area is the positive correlation between $CO_2/^4He$ and 1/He, with an R^2 of 0.97 (Fig. 4a). This indicates that the addition of CO_2-rich fluids is a likely cause, that these samples are far from the range of ^{4}He-rich fluids in the crust, and that there may be a CO_2-rich reservoir at depth. From the estimated reservoir temperature (Table S2) and geothermal gradient of 3.5 °C/100 m, it is inferred that the depth of the CO_2 reservoir is >10 km, which is consistent with carbonate metamorphism and decarbonization. However, a mixing relationship with mantle CO_2 (Fig. 4b) was not evident, which is consistent with the estimated mantle carbon ratio (most samples) of <5 %. Based on the systematic correlation of He–C, $CO_2/^3He$ is negatively correlated with $^3He/^4He$ (Fig. 4c). This may be due to contamination by crustal materials. Given that samples with low $^3He/^4He$ values have higher $CO_2/^3He$ values, this mixture is likely to be AOC. Magmatic degassing and calcite precipitation can reduce $CO_2/^3He$, but cannot explain the negative correlation between $CO_2/^3He$ and $^3He/^4He$. From the helium–carbon coupling model, the samples were surrounded by the DMM, AOC, and CC mixing curves. Considering the evolution process of the two stages, the different proportions of the three end elements can be estimated. The end elements of the DMM, AOC, and CC in the five blocks were 10 %, 50 %, and 40 %, respectively. The TCB and TPSE had a slightly higher mantle carbon proportion (~15 %), whereas DZB mantle carbon was <5 % (Table S1 and Table S2). Therefore, based on the data, CO_2-type gas in this study was mainly controlled by crust–mantle mixing, which provides an opportunity for us to constrain carbon recycling (Fig. 4; Ray et al., 2009; Buttitta et al., 2023).

4.2. Geographical distribution of $^3He/^4He$ ratios and helium flux

The distribution of $^3He/^4He$ ratios provides crucial insights into regional crust–mantle interactions and helps identify conduits of mantle volatiles through the crust. A total of 376 sites with helium isotope ratios revealed significant boundaries after excluding data possibly influenced by air contamination during sampling (Fig. 2a and Fig. 3). There were remarkably high helium ratios (2.36 ± 0.7 R_A, Guanding) at the intersection of the XSHF and XJF, as well as an anomalously value (5.15 ± 0.1R_A, Qingping) observed at the bend between the JSF and RRF. Although several other locations along the XSHF and RRF also exhibited clear mantle helium signals (<2 R_A), these two bend sites with particularly prominent mantle helium anomalies indicate a significant contribution of primordial ^{3}He carried by ascending magmas from the mantle. Crucially, a distinct mantle helium signal was also detected in the hot springs at the southern of the LXF (0.37 ± 0.15 R_A, Xiamiandian), where tensive strain occurs in the predominantly thrusting system, which is an unfavorable condition for the transfer of mantle helium (Zhang et al., 2021). These results suggest that it is difficult for the crust to block the release of deep mantle helium even under the action of a high-stress within crust. Therefore, along the line where the

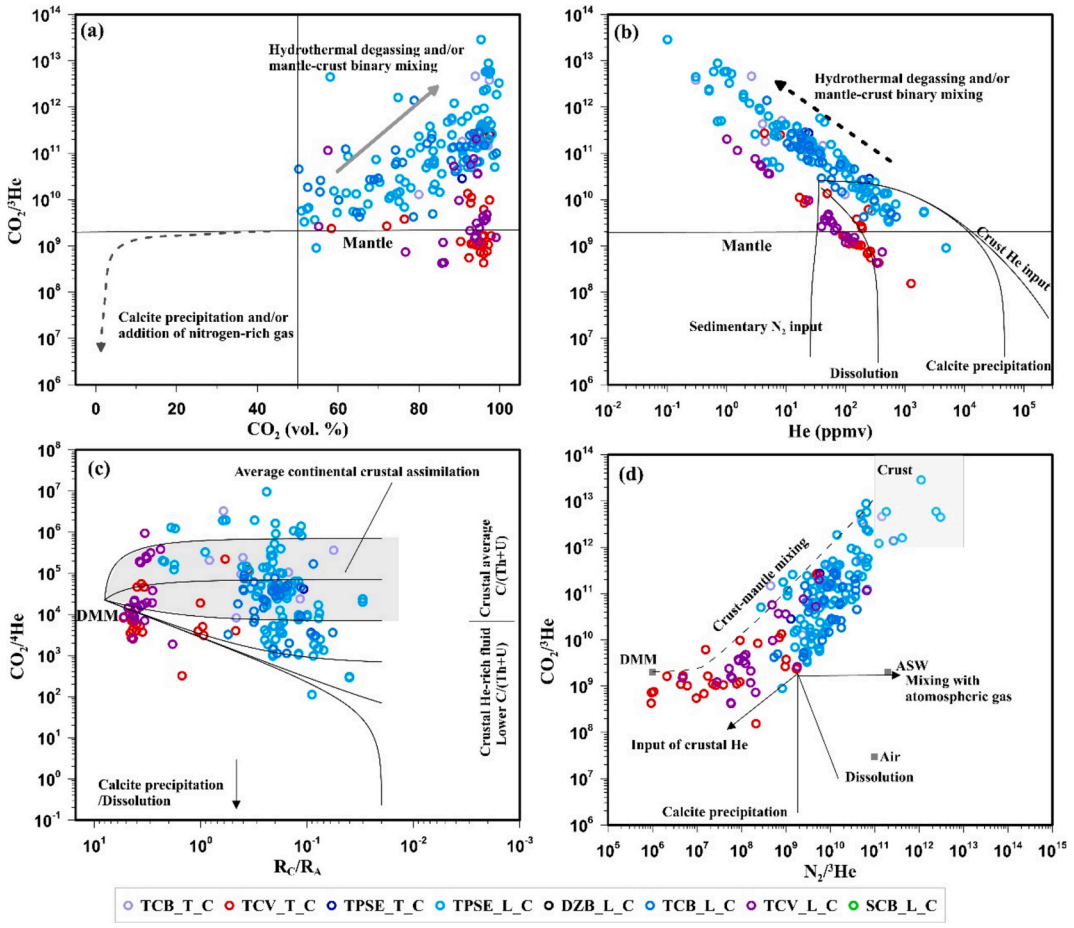

Fig. 3. Plots of (a) $CO_2/^3He$ vs. CO_2, (b) $CO_2/^3He$ vs. He, (c) $CO_2/^4He$ vs. $^3He/^4He$, and (d) $CO_2/^3He$ vs. $N_2/^3He$ for hot spring gas of the five blocks of the southeastern Tibetan Plateau. Grey circles represent typical DMM and air/ASW endmember values from Sano and Marty (1995). Dotted lines in (a) suggest the input of He-rich fluids with the DMM as a starting point. The processes of dissolution (Gilfillan et al., 2009), calcite precipitation, and input of crustal radiogenic ^4He (Hao et al., 2023) are shown by solid gray lines in (a) and (b).

LXF intersects the XSHF and RRF, we discovered a helium anomaly boundary zone (HBZ). Considering the geological and geophysical results, the alignment of the HBZ suggests slab tearing, which provides a pathway for mantle helium upwelling (Fig. 7). The location of the tearing slab inferred from the helium isotope ratio anomaly is consistent with the results of recent P- and S-wave seismic tomography (Fig. 8, Fig. S4, and Fig. S5; Hou et al., 2024). In addition, strontium isotope and neodymium contour maps of magmatic rocks from this area (24°–28°N, 98°–102°E) show an east–north anomaly near 26°N (Fig. S6; Li et al., 2024b; Tang et al., 2024).

Conversely, helium ratios decrease significantly south of the LXF, particularly within the DZB, where there is almost no mantle helium signal. This reduction in the helium ratio is closely related to the nature of the XJF within the crust of the DZB, which shares cratonic characteristics similar to those of the SCB (Wang et al., 2021). Notably, at the intersection of the XJF and RRF, a clear mantle helium signal was detected, which was attributed to the influence of the RRF. Geochemical data also indicate that the XJF is confined within the crust, whereas the RRF penetrates the lithospheric mantle (Shao et al., 2024). The helium signal was predominantly crustal within the SCB. However, it was challenging to constrain the slab morphology because the number of samples was limited (n = 4).

The samples of the five blocks and other non-volcanic hydrothermal systems in the study area all spanned five orders of magnitude, among which TCV was in the range of typical "volcanic" degassing, TCB was in the range of typical "volcanic" to typical "tectonic" areas, and TPSE, DZB, and SCB were in the range of "tectonic" areas (Fig. 5). This shows that the hydrothermal system in the tectonic region contributes more to the mantle helium. The average mantle ^3He and ^4He fluxes of the TCV were 2.1×10^5 (range 6.5×10^4 – 3.2×10^5 atoms m^{-2} s^{-1}) and 4.1×10^{10} atoms m^{-2} s^{-1} (range 1.2×10^{10} – 6.1×10^{10} atoms m^{-2} s^{-1}), respectively, comparable to typical volcanic areas around the world (10^4–10^9 atoms m^{-2} s^{-1} for mantle ^3He flux and 10^9–10^{14} atoms m^{-2} s^{-1} for mantle ^4He flux) (Moreira and Kurz, 2013). The average mantle ^3He flux and ^4He flux were 1.7×10^4 atoms m^{-2} s^{-1} and 2.8×10^9 atoms m^{-2} s^{-1} for TPSE and 1.4×10^4 atoms m^{-2} s^{-1} and 1.95×10^9 atoms m^{-2} s^{-1} for TCB, and 1.04×10^4 atoms m^{-2} s^{-1} and 2.52×10^9 atoms m^{-2} s^{-1} for DZB, respectively, which can be compared with typical continental degassing (10^1–10^7 atoms m^{-2} s^{-1} for mantle ^3He flux and 10^6–10^{12} atoms m^{-2} s^{-1} for mantle ^4He flux) (Torgersen, 2010). From the relationship between ^4He flux in mantle and ^4He flux in crust, tectonic activity in the study area is the main process of helium degassing from mantle. The TPSE (north of the LXF) and TCB (west) have the highest ^3He fluxes (Table S3, Fig. 5, and Fig. S7), whereas the DZB and SCB are dominated by crustal ^4He fluxes. These average flux values for each block represent the different characteristics of the southeastern Tibetan Plateau. Local anomalies are possible near the Nandinghe fault zone in the TCB, and areas of high ^4He flux result from regional geology and fault interactions, possibly influenced by complex water–gas interactions (Wang et al., 2023). Overall, the five blocks can be classified into group 1 (TCV), group 2 (TPSE and TCB), and group 3 (DZB and SCB) based on their distinct helium inventory and flux characteristics.

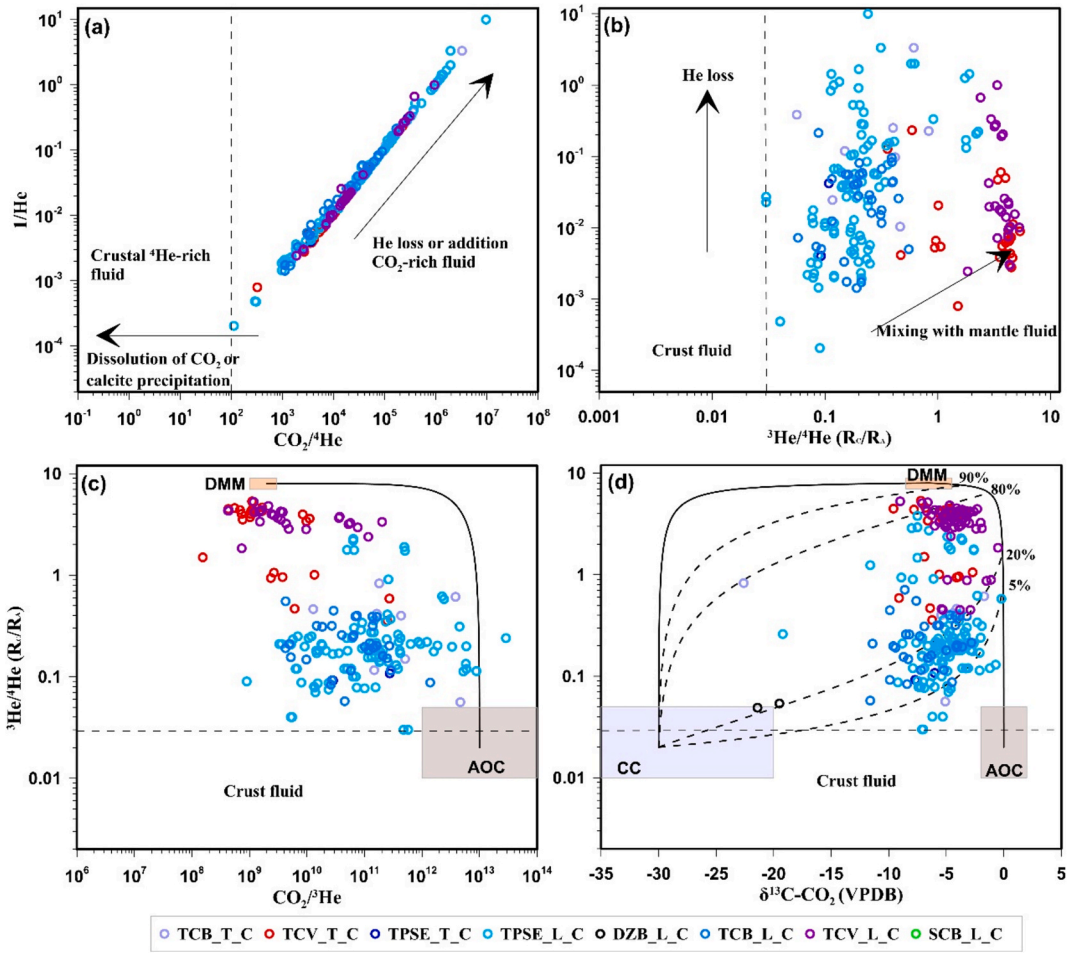

Fig. 4. He–CO_2 systematics. (a) $CO_2/^4He$ vs. 1/He and (b) $^3He/^4He$ (R_C/R_A) vs. 1/He. CO_2-type gas shows a significant mixing trend with mantle fluid. The initially exsolved gases from crustal fluid reservoir are defined according to the geochemical tendency of the samples. Crustal ^4He-rich fluids are expected to have lower $CO_2/^4He$ than are mantle fluids, reflecting excess ^4He relative to CO_2. (c) $^3He/^4He$ (R_C/R_A) vs. $CO_2/^4He$; note that in some cases the $\delta^{13}C$–CO_2 value of mantle fluids could be comparable with that of the mixture between crustal reduced and oxidized carbon. (d) $^3He/^4He$ (R_C/R_A) vs. $\delta^{13}C$–CO_2 (‰), showing two-stage evolution using the He–C coupling model and values for the DMM, AOC, and CC end-members (Table 1).

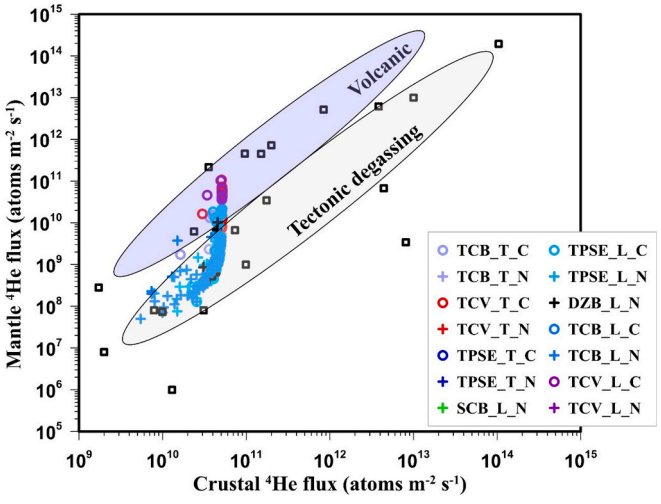

Fig. 5. Mantle ^4He flux vs. crust ^4He flux in study area based on a porosity of 1%. Pink shading represents the range of volcanic helium degassing, and gray shading represents the range of tectonic helium degassing. Hollow square represents data from Torgersen (2010) and Hao et al. (2024).

4.3. Spatial characteristics of helium–carbon and the subduction slab

The refined He–CO_2 coupling model considered a two-stage evolution process for CO_2 (Text S2 and Table 1; Van Soest et al., 1998; Li et al., 2020a). Previous studies highlight significant CC in the region, with $\delta^{13}C$-CO_2 and $^3He/^4He$ values of − 7.7 ‰ ± 1.6 ‰ and 0.03 ± 0.01 R_A, respectively. Subduction carries carbonates and organic sediments, considered as AOC, which decarbonate and rise through faults into hydrothermal systems (recycled carbon; Lopez et al., 2023). The two-stage carbon model for recycled carbon is detailed in the supplementary materials. Our results show that the TCV has 37 % recycled carbon, TPSE approximately 35 %, and TCB approximately 24 %, while DZB and SCB have 22 % and 14 %, respectively (Fig. 6), which are controlled by different tectonic activities.

Helium and carbon isotopes along with the AOC ratios of hot springs within 30 km of the XSHF and RRF were analyzed. The helium boundary south of the LXF marks the major channel for mantle helium upwelling (Fig. 7). The northern segment of the XSHF (labeled 1 in Fig. 7a), likely represents the leading edge of the Indian lithospheric slab based on helium data and geophysical results (Dong et al., 2020). The helium boundary of 2nd and 3rd segments is clear based on the isotope ratio, while that of the 4th segment is based on the model proposed by Hou et al. (2024). This helium boundary line is supported by the (1) LXF thrust dividing the TPSE and DZB block; (2) TPSE being characterized by more mantle helium than is the DZB (Fig. 7e); (3) TPSE having a higher

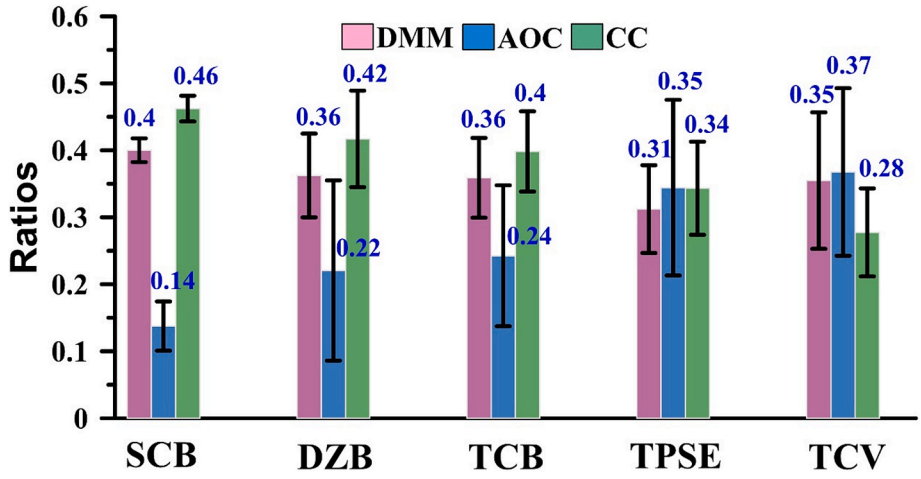

Fig. 6. Average proportions of the three endmember elements of regional carbon emissions in the five blocks. The proportion of AOC is 0.35 in TPSE, and 0.22 in DZB, showing a distinct difference.

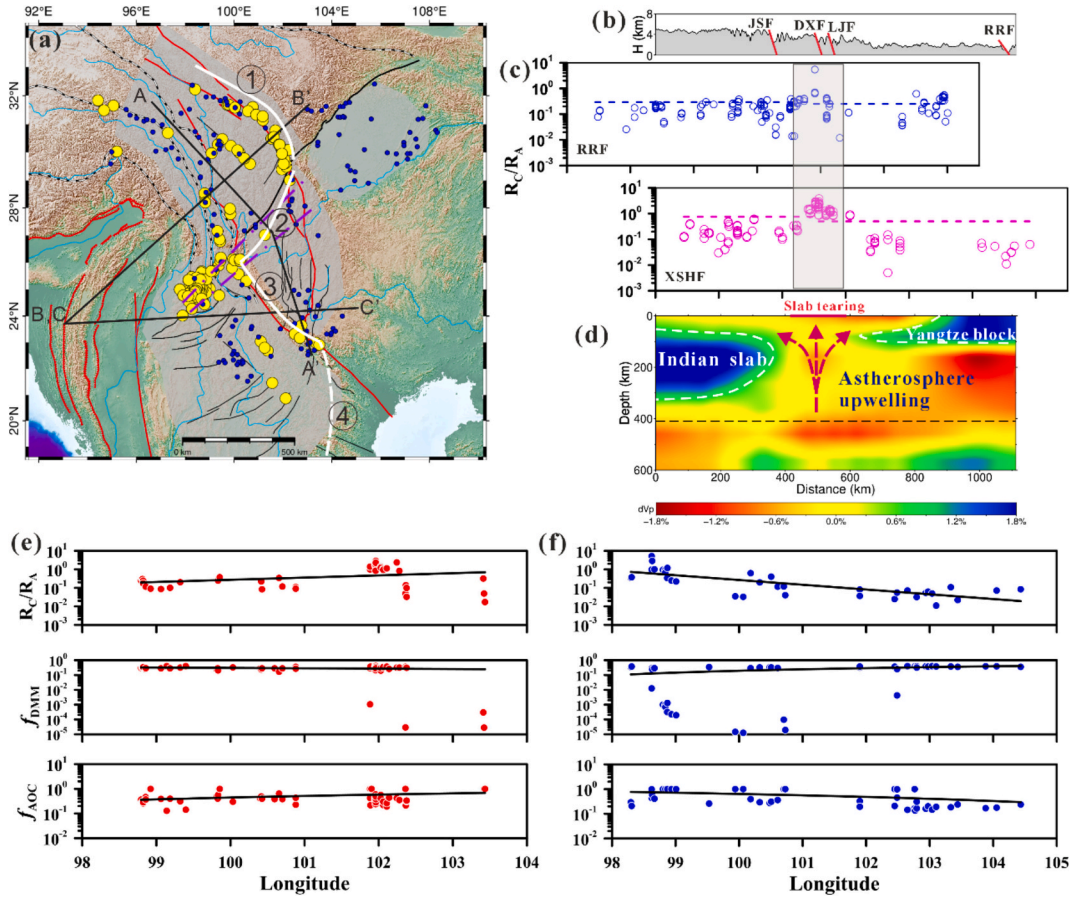

Fig. 7. (a) Helium boundary of the southeastern Tibetan Plateau and seismic profiles A–A', B–B', and C–C'. (b) Topography profile of A–A' in (a). (c) The R_C/R_A transect profile along the RRF (blue cycle) and XSHF (red cycle); shaded area shows the slab tearing belt. (d) P-wave structures along profile A–A' (modified from Hou et al., 2024 with permission from Springer Nature). (e) and (f) are values of R_C/R_A, f_{DMM} and f_{AOC} transects along profiles B–B' and C–C', respectively.

ratio of recycled carbon than does the DZB (Fig. 7f). Isotopic data profiles show a north–south division, indicating lithospheric slab tearing near 26°N (Li et al., 2024b). The Indian lithospheric mantle subducts at a low angle north of the boundary (2nd segment), whereas the subduction is steeper and deeper south of that (Hou et al., 2024; Li et al., 2024b).

The junction points (southeast of DZB) of the XSHF, RRF, and LXF faults might have high permeability for mantle helium release. However, the XSHF and RRF are strike-slip faults under compression, and the LXF is a thrust fault, all experiencing high strain at intersections, indicating that the junctions are not more permeable than other fault segments (Zhang et al., 2021; Newell et al., 2023). Permeability appears consistent along the fault zone, as shown by the lack of correlation between R_C/R_A, $\delta^{13}C\text{-}CO_2$, recycled AOC ratio, total strain rate, and crustal thickness (Fig. S8). We derived the mantle helium and carbon anomalies

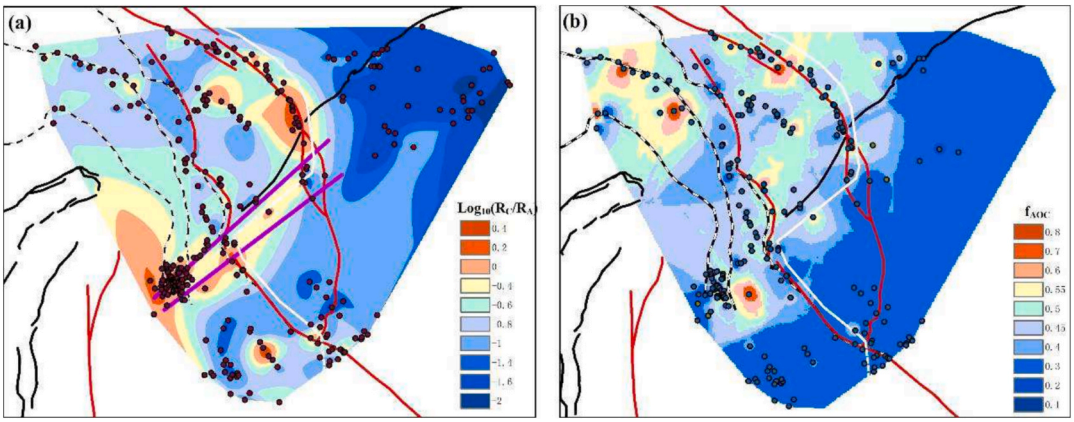

Fig. 8. (a) Contour map of helium isotope ratios in the study area. The apparent high helium isotope ratio band on the southern side of the LXF is consistent with the tearing slab region (dashed yellow lines, Fig. 1b) revealed by P-wave velocity imaging (Hou et al., 2024). (b) Contour map of AOC ratios showing a distinct carbon boundary.

Table 1
Summary parameters of the He–C coupling model for the three end-members.

	C (ppm)	$\delta^{13}C$ (‰)	He (ppm)	R_C/R_A
Depleted mantle, DMM	700[a]	-6.5 ± 2.5[b]	0.0288[c]	8 ± 1[b]
Altered oceanic crust, AOC	11,400[d]	0.3 ± 1[e]	0.00023[d]	0.02[b]
Crustal carbon, CC	8500[a]	-7.7 ± 1.6[f]	0.204[f]	0.03 ± 0.01[f]

Note. a. (Lopez et al., 2023); b. (Sano and Fischer, 2013); c. (Zhang et al., 2016); d. (Hoefs, 2021); e. (Van Soest et al., 1998); f. This study, calculated by the average value of $CO_2/^3He$, $^3He/^4He$ (R_C/R_A) and $\delta^{13}C$-CO_2.

along the XSHF and RRF, which were controlled by lithospheric slab tearing at depth.

The helium isotope ratio offers a unique tracer of crust–mantle interactions. According to the contour map of hot spring helium isotope ratios in the study area (Fig. 8), there is a clear band of high helium isotope ratios south of LXF, and high ratios in the Tengchong volcano area. This band of high helium isotope ratios is consistent with seismic imaging (Hou et al., 2024). In addition, the contours of the AOC ratio on both sides of the helium boundary show a clear boundary, indicating the controlling effect of plate-tearing morphology on AOC cycling carbon.

In addition to AOC, the variation ratio of mantle carbon along the LXF (Table S2) indicates that metasomatized lithospheric mantle of the Indian continental plate may serve as a potential reservoir for deep volatiles (Aulbach et al., 2013; Aulbach et al., 2017; Kovács et al., 2021). Geophysical and geochemical studies have shown that the Indian lithospheric mantle has experienced pervasive metasomatism by sediment-derived fluids and melts, leading to enrichment in incompatible elements and volatiles (Zhou et al., 2012; Zhu et al., 2021; Dong et al., 2022). This metasomatized lithospheric mantle can release CO_2-rich volatiles when subjected to thermal perturbation or mechanical disintegration during lithospheric tearing, foundering, or underthrusting processes (Cloetingh et al., 2021; Gorczyk and Gonzalez, 2019; Tang et al., 2025; Wang et al., 2017). In the Tengchong volcanic field and southeastern Tibetan Plateau, multiple geochemical indicators—including low $\delta^{26}Mg$, low $\delta^{44}/^{40}Ca$, elevated Ba/Th, and enriched Sr–Nd–Pb isotopes—suggest a mantle source modified by Indian carbonate-rich sediments and lithospheric materials (Liu et al., 2017; Tian et al., 2018). These signatures are interpreted as evidence of slab-derived supercritical fluids and dolomitic components metasomatizing the overlying mantle wedge at depths of 120–300 km (Liu et al., 2017; Tian et al., 2018). Given that slab tearing enhances asthenospheric upwelling and exposes the lower lithosphere to decompression and heating, it is plausible that such processes promote CO_2 release from the hydrated and carbonated Indian lithosphere near the tear edge (Fig. 9a; Aulbach et al., 2017; Lange et al., 2023). Notably, recent Mg–Ca isotope models estimated that 5 %–8 % of dolostone was incorporated into the mantle beneath Tengchong, further indicating significant carbonate recycling in this region (Liu et al., 2017). Nonetheless, it remains challenging to conclusively determine whether the carbon source originated from the Indian lithospheric mantle and/or AOC. Further research is required to provide a more comprehensive understanding of carbon source models.

4.4. Slab tearing and its geodynamic implications

Geodynamic models related to the uplift of the southeastern Tibetan Plateau include the rigid block extrusion model (Tapponnier et al., 2001), continuous deformation model (England and Houseman, 1986), crustal flow model (Clark and Royden, 2000) and slab-tearing model (Hou et al., 2024). The material in the Plateau interior moves southeast, whereas the Yangtze Plate blocks eastward movement and causes southeast clockwise rotation (Wang et al., 2014). The DZB bounded by the LXF is crucial for responding to the eastward movement (Liu et al., 2014). The southeastern margin of the plateau is divided by large strike-slip faults such as the XSHF and RRF, resulting in intense tectonic activity and frequent seismicity (Wang et al., 2021). The tearing of the Indian lithospheric slab beneath eastern Tibet triggers diverging subduction, facilitating material movement and rotation and resulting in differential eastward growth.

Geochemical evidence (helium isotope ratios) for slab tearing of the Indian subducting plate is consistent with seismic tomographic observations and provides insights into the uplift of the southeastern Tibetan Plateau (Fig. 9). Across the Tibetan Plateau and southeastern Asia, tomography profiles show significant lateral variations in the subducting Indian lithosphere, reflecting the complex tectonic processes of the subducting Indian lithosphere from west to east and southeast. In the southeastern EHS and Indo–Burma Range, a prominent high-velocity tomographic anomaly trending NW–SE has been observed along the plate boundary (Raoof et al., 2017; Yao et al., 2021). This anomaly corresponds to the ongoing eastward subduction of the Indian lithosphere beneath Burma and western Yunnan (Fig. 9a; Replumaz et al., 2010; Raoof et al., 2017; Ding et al., 2022; Hou et al., 2024). Local discontinuities in the high-velocity body beneath the Indo–Burma range suggest slab tearing in the subducted Indian lithosphere (Raoof et al., 2017; Bian et al., 2022; Ding et al., 2022; Hou et al., 2024). P-wave anomaly maps and cross-sectional profiles across the EHS and Indo–Burma Range highlight this tearing, which plays a crucial role in shaping the lithospheric structures in southeastern Asia (Raoof et al., 2017; Ding et al., 2022). Seismic tomography suggests that sub-vertical slab tears in the EHS are associated with distinctive magmatic signatures, such as potassic igneous rocks ranging from mafic to felsic

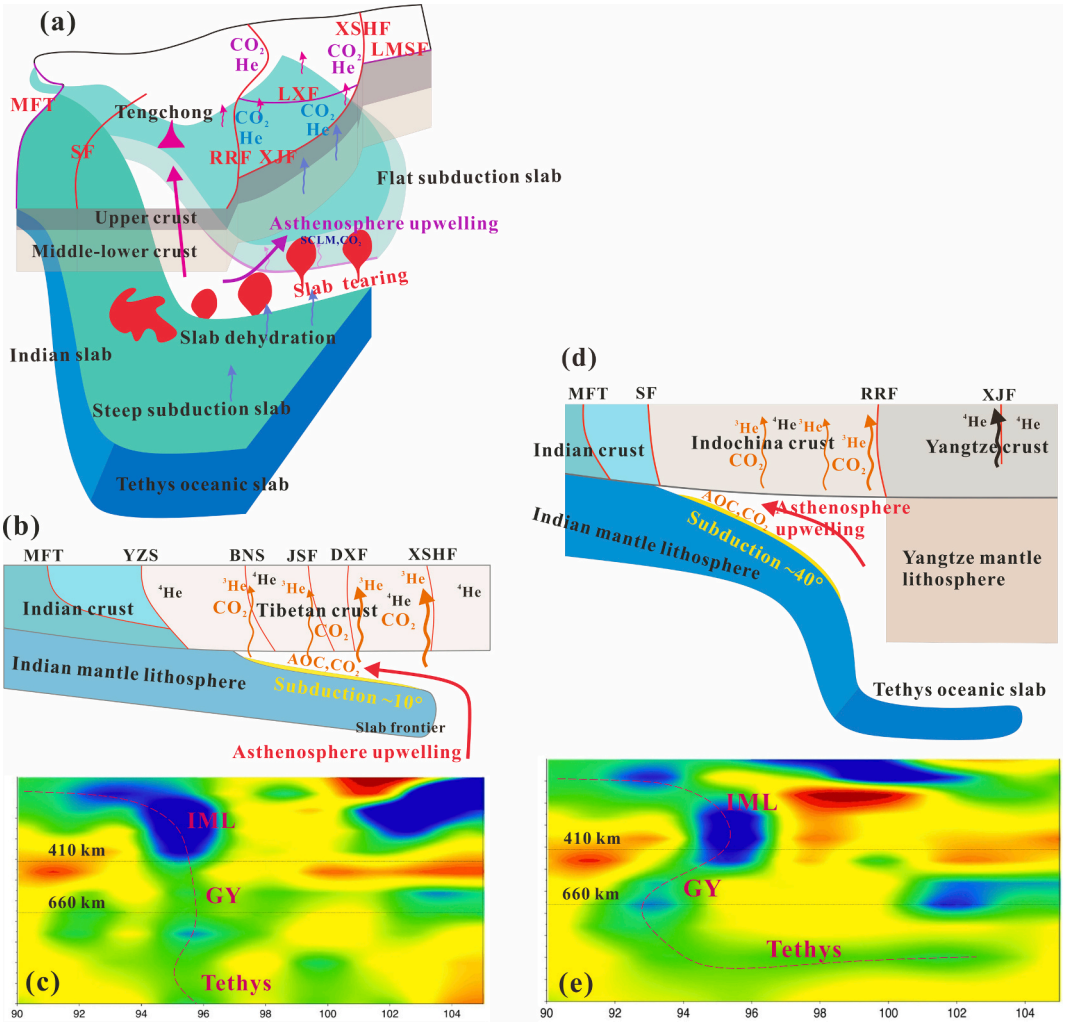

Fig. 9. Schematic diagram showing slab tearing and controls on carbon recycling south of the LXF on the southeastern Tibetan Plateau. South of this fault system, the Indian slab undergoes steep, deep subduction, while to the north, it experiences gentler, shallower subduction (Yao et al., 2021). (c) and (e) Seismic tomographic profiles of B–B' and C–C' (in Fig. 7), respectively, in the eastern Tibetan Plateau (modified from Hou et al., 2024 with permission from Springer Nature), showing the subducting slab still connected with the surface plate.

compositions, faulting, and block rotation (Lu et al., 2012; Li et al., 2017; Bian et al., 2022).

Slab tearing was also supported by evidence from Eocene–Oligocene potassic felsic intrusions, rapid block rotations (40–20 Ma), and mantle anisotropy derived from GPS and seismic data. The tearing of the subducting slab induces toroidal mantle flow, as observed in the SKS splitting and seismic anisotropy data, and facilitates asthenospheric material influx beneath the EHS (Chen et al., 2015; Zhou et al., 2019). This mantle upwelling causes localized heating, partial melting of the extending crust, and thermal advection, leading to the formation of NW–SE dextral strike-slip shear zones. These zones bend into N–S and NE–SW orientations near the syntaxis, merging with the Sagaing Fault (Li et al., 2017; Ding et al., 2022). Paleomagnetic and kinematic evidence suggests that the clockwise rotation of crustal blocks in southeastern Tibet is a direct consequence of slab tearing and subsequent mantle flow (Li et al., 2017; Gan et al., 2021; Ding et al., 2022). However, in southeastern Tibet, the development of a V-shaped conjugate shear system reflects the unique geographic and tectonic conditions. The sinistral shear zone of the Ailaoshan Red River, combined with the dextral zones, forms the largest system in the region. In western Yunnan, Tertiary potassic felsic magmatism (~38–32 Ma; Lu et al., 2012) is linked to lithospheric mantle and asthenospheric upwelling during the Eocene (Omrani et al., 2008; Hou et al., 2024). This upwelling facilitated by slab tearing can produce adakitic magmatism, thermal anomalies, and lateral mantle flow perturbations (Li et al., 2017).

Based on geological and geophysical data from the southeastern EHS and surrounding regions, we propose a deformation model for the crust, and a slab tear in the subducting Indian lithosphere beneath the EHS. This model reconstructs the morphology and structure of the Indian Plate beneath the Tibetan Plateau and Indo–Burma Range. Additionally, high-velocity anomalies suggest that the Indian lithosphere is torn beneath the EHS, with ruptures extending to depths of ~600 km beneath the Indo–Burma Range (Fig. 9c, e; Raoof et al., 2017; Hou et al., 2024). Slab tearing triggers diverging subduction and is crucial for carbon recycling at convergent boundaries (Bekaert et al., 2021; Zhang et al., 2024). The subduction of the Indian lithosphere beneath southern Tibet controls crustal metamorphic CO_2 and mantle degassing (Li et al., 2024a). The escaped material in the southeastern Tibetan Plateau is blocked by the craton-like DZB, causing lithospheric tearing and differential subduction north and south around the LXF, which controls element cycling. The carbon recycling ratio is 35 % to the north and 22 % to the south of the LXF, based on the calculated AOC ratio (Table S2), suggesting that subduction morphology controls volatile recycling.

The TCV is a Cenozoic intraplate volcano on the southeastern Tibetan Plateau, and its magmatic source has been debated (Lei and Zhao, 2016; Zou et al., 2017; Tian et al., 2018; Wang et al., 2025). Our data

suggest that the tearing slab forms a slab window that allows localized mantle upwelling to recharge the TCV. This magma may be related to the partial melting of the enriched mantle wedge, resulting in slab detachment from the subducting Indian slab, according to geochemical and numerical model simulation results (Zhang et al., 2017). This interpretation contradicts earlier models that attributed the TCV to slab dehydration within the mantle transition zone, differentiating it from volcanoes of the Changbai Mountains (Zhu et al., 2019).

5. Conclusions

This study presents a spatial analysis of gas compositions and isotopes (He-C) from 376 hot springs (905 samples) on the southeastern Tibetan Plateau combined with a two-stage He–CO_2 evolution model, and investigates the inventories of helium and carbon, as well as their evolutionary processes. The distribution and variation patterns of helium flux, carbon flux, and recycled AOC ratio along the fault zones (RRF and XSHF) were characterized. We identified the presence of slab tearing in the Indian lithosphere slab south of the LXF according to helium isotope geochemical perspective for the first time. This slab tearing provides new insights into the uplift mechanisms of the southeastern Tibetan Plateau, control of carbon recycling efficiency at convergent plate boundaries, and origin of intraplate volcanic magmatism.

CRediT authorship contribution statement

Yingchun Wang: Writing – original draft, Software, Investigation. **Xiaocheng Zhou:** Project administration, Methodology, Funding acquisition. **Jiao Tian:** Writing – review & editing, Conceptualization. **Pengfei Chen:** Resources. **Miao He:** Writing – review & editing. **Yucong Yan:** Resources. **Bingyu Yao:** Writing – review & editing. **Zhongping Li:** Investigation. **Chunhui Cao:** Investigation. **Hikaru Iwamori:** Writing – review & editing, Methodology.

Declaration of competing interest

The authors declare that they have no known competing financial interests or personal relationships that could have appeared to influence the work reported in this paper.

Acknowledgments

This work was funded by the Deep Earth Probe and Mineral Resources Exploration - National Science and Technology Major Project (2024ZD1000503), the National Key Research and Development Project (2023YFC3012005-1), Central Public-Interest Scientific Institution Basal Research Fund (CEAIEF20240405, CEAIEF2022030200, CEAIEF2022030205, CEAIEF20240207), the National Natural Science Foundation of China (41673106, 41403099), and IGCP Project 724. Y. Wang acknowledges support from the China Scholarship Council (202208510118). We thank Wenbin Zhao from the Institute of Geology and Geophysics, Chinese Academic Sciences, for providing early research materials for the He–C coupling model, and Prof. Antonio Caracausi from the Istituto Nazionale di Geofisica e Vulcanologia for valuable suggestions and thoughtful discussions on the manuscript. We extend our appreciation to the editors, and Prof. Sierd Cloetingh, and an anonymous reviewer for their thorough and constructive comments.

Data availability

The data supporting the findings of this study are available from Jia (2024). Previously published data and corresponding papers were compiled and are available in the Supplementary Materials and Zenodo dataset https://doi.org/10.5281/zenodo.13407358.

Appendix A. Supplementary data

Supplementary data to this article can be found online at https://doi.org/10.1016/j.gr.2025.06.001.

References

Asaah, A.N.E., Yokoyama, T., Aka, F.T., Usui, T., Kuritani, T., Wirmvem, M.J., Iwamori, H., Fozing, E.M., Tamen, J., Mofor, G.Z., Ohba, T., Tanyileke, G., Hell, J.V., 2015. Geochemistry of lavas from maar-bearing volcanoes in the Oku Volcanic Group of the Cameroon Volcanic Line. Chem. Geol. 406, 55–69. https://doi.org/10.1016/j.chemgeo.2015.03.030.

Aulbach, S., Griffin, W.L., Pearson, N.J., O'Reilly, S.Y., 2013. Nature and timing of metasomatism in the stratified mantle lithosphere beneath the central Slave craton (Canada). Chem. Geol. 352, 153–169. https://doi.org/10.1016/j.chemgeo.2013.05.037.

Aulbach, S., Sun, J., Tappe, S., Höfer, H.E., Gerdes, A., 2017. Volatile-rich metasomatism in the cratonic mantle beneath SW Greenland: link to kimberlites and mid-lithospheric discontinuities. J. Petrol. 58 (12), 2311–2338. https://doi.org/10.1093/petrology/egy009.

Bai, D., Unsworth, M.J., Meju, M.A., Ma, X., Teng, J., Kong, X., Sun, Y., Sun, J., Wang, L., Jiang, C., Zhao, C., Xiao, P., Liu, M., 2010. Crustal deformation of the eastern Tibetan plateau revealed by magnetotelluric imaging. Nat. Geosci. 3 (5), 358–362. https://doi.org/10.1038/ngeo830.

Ballentine, C.J., Burnard, P.G., 2002. Production, release and transport of noble gases in the continental crust. Rev. Mineral. Geochem. 47 (1), 481–538. https://doi.org/10.2138/rmg.2002.47.12.

Barry, P.H., Hilton, D.R., Fischer, T.P., de Moor, J.M., Mangasini, F., Ramirez, C., 2013. Helium and carbon isotope systematics of cold "mazuku" CO_2 vents and hydrothermal gases and fluids from Rungwe Volcanic Province, southern Tanzania. Chem. Geol. 339, 141–156. https://doi.org/10.1016/j.chemgeo.2012.07.003.

Barry, P.H., Negrete-Aranda, R., Spelz, R.M., Seltzer, A.M., Bekaert, D.V., Virrueta, C., Kulongoski, J.T., 2020. Volatile sources, sinks and pathways: A helium-carbon isotope study of Baja California fluids and gases. Chem. Geol. 550, 119722. https://doi.org/10.1016/j.chemgeo.2020.119722.

Becker, J.A., Bickle, M.J., Galy, A., Holland, T.J.B., 2008. Himalayan metamorphic CO_2 fluxes: quantitative constraints from hydrothermal springs. Earth Planet. Sci. Lett. 265 (3), 616–629. https://doi.org/10.1016/j.epsl.2007.10.046.

Bekaert, D.V., Turner, S.J., Broadley, M.W., Barnes, J.D., Halldórsson, S.A., Labidi, J., Wade, J., Walowski, K.J., Barry, P.H., 2021. Subduction-driven volatile recycling: A global mass balance. Annu. Rev. Earth Planet. Sci. 49 (49), 37–70. https://doi.org/10.1146/annurev-earth-071620-055024.

Bian, S., Gong, J., Zuza, A.V., Yang, R., Chen, L., Ji, J., Yu, X., Tian, Y., Yu, Z., Cheng, X., Lin, X., Chen, H., 2022. Along-strike variation in the initiation timing of the north-trending rifts in southern Tibet as revealed from the Yadong-Gulu Rift. Tectonics 41 (7), e2021TC007091. https://doi.org/10.1029/2021TC007091.

Burnard, P.G., Hu, R., Turner, G., Bi, X.W., 1999. Mantle, crustal and atmospheric noble gases in ailaoshan gold deposits, Yunnan Province, China. Geochim. Cosmochim. Acta 63 (10), 1595–1604. https://doi.org/10.1016/S0016-7037(99)00108-8.

Buttitta, D., Capasso, G., Paternoster, M., Barberio, M.D., Gori, F., Petitta, M., Picozzi, M., Caracausi, A., 2023. Regulation of deep carbon degassing by gas-rock-water interactions in a seismic region of Southern Italy. Sci. Total Environ. 897, 165367. https://doi.org/10.1016/j.scitotenv.2023.165367.

Caracausi, A., Buttitta, D., Picozzi, M., Paternoster, M., Stabile, T.A., 2022. Earthquakes control the impulsive nature of crustal helium degassing to the atmosphere. Commun. Earth Environ. 3 (1), 224. https://doi.org/10.1038/s43247-022-00549-9.

Caracausi, A., Sulli, A., 2019. Outgassing of mantle volatiles in compressional tectonic regime away from volcanism: the role of continental delamination. Geochem. Geophys. Geosyst. 20 (4), 2007–2020. https://doi.org/10.1029/2018GC008046.

Chen, Y., Li, W., Yuan, X., Badal, J., Teng, J., 2015. Tearing of the Indian lithospheric slab beneath southern Tibet revealed by SKS-wave splitting measurements. Earth Planet. Sci. Lett. 413, 13–24. https://doi.org/10.1016/j.epsl.2014.12.041.

Clark, M.K., Royden, L.H., 2000. Topographic ooze: Building the eastern margin of Tibet by lower crustal flow. Geology 28 (8), 703–706. https://doi.org/10.1130/0091-7613(2000)28<703:TOBTEM>2.0.CO;2.

Clift, P.D., 2017. A revised budget for Cenozoic sedimentary carbon subduction. Rev. Geophys. 55 (1), 97–125. https://doi.org/10.1002/2016RG000531.

Cloetingh, S., Koptev, A., Kovács, I., Gerya, T., Beniest, A., Willingshofer, E., Ehlers, T.A., Andrić-Tomašević, N., Botsyun, S., Eizenhöfer, P.R., François, T., Beekman, F., 2021. Plume-induced sinking of intracontinental lithospheric mantle: an overlooked mechanism of subduction initiation? Geochem. Geophys. Geosyst. 22 (2), e2020GC009482. https://doi.org/10.1029/2020GC009482.

Correale, A., Paonita, A., Rizzo, A., Grassa, F., Martelli, M., 2015. The carbon-isotope signature of ultramafic xenoliths from the Hyblean Plateau (southeast Sicily, Italy): evidence of mantle heterogeneity. Geochem. Geophys. Geosyst. 16 (3), 600–611. https://doi.org/10.1002/2014GC005656.

Crossey, L.J., Karlstrom, K.E., Springer, A.E., Newell, D., Hilton, D.R., Fischer, T., 2009. Degassing of mantle-derived CO_2 and He from springs in the southern Colorado Plateau region—Neotectonic connections and implications for groundwater systems. GSA Bull. 121 (7–8), 1034–1053. https://doi.org/10.1130/B26394.1.

Day, J.M.D., Barry, P.H., Hilton, D.R., Burgess, R., Pearson, D.G., Taylor, L.A., 2015. The helium flux from the continents and ubiquity of low-$^3He/^4He$ recycled crust and lithosphere. Geochim. Cosmochim. Acta 153, 116–133. https://doi.org/10.1016/j.gca.2015.01.008.

Ding, L., Kapp, P., Cai, F., Garzione, C.N., Xiong, Z., Wang, H., Wang, C., 2022. Timing and mechanisms of Tibetan Plateau uplift. Nat. Rev. Earth Environ. 3 (10), 652–667. https://doi.org/10.1038/s43017-022-00318-4.

Dong, P., Dong, G., Santosh, M., Mo, X., Sun, Z., Ketchaya, Y.B., Pan, Y., Lemdjou, Y.B., 2022. Eocene magmatism in the western Tengchong Block: Implications for crust-mantle interaction associated with the slab rollback of the Neo-Tethys Ocean. Gondwana Res. 106, 259–280. https://doi.org/10.1016/j.gr.2022.01.018.

Dong, H., Wei, W., Jin, S., Ye, G., Zhang, L., Jing, J.E., Yin, Y., Xie, C., Jones, A.G., 2016. Extensional extrusion: Insights into south-eastward expansion of Tibetan Plateau from magnetotelluric array data. Earth Planet. Sci. Lett. 454, 78–85. https://doi.org/10.1016/j.epsl.2016.07.043.

Dong, X., Yang, D., Zhu, H., 2020. Adjoint tomography of the lithospheric structure beneath Northeastern Tibet. Seismol. Res. Lett. 91 (6), 3304–3312. https://doi.org/10.1785/0220200135.

England, P., Houseman, G., 1986. Finite strain calculations of continental deformation: 2. Comparison with the India-Asia collision zone. J. Geophys. Res. Solid Earth 91 (B3), 3664–3676. https://doi.org/10.1029/JB091iB03p03664.

Foley, S.F., Fischer, T.P., 2017. An essential role for continental rifts and lithosphere in the deep carbon cycle. Nat. Geosci. 10 (12), 897–902. https://doi.org/10.1038/s41561-017-0002-7.

Gan, W., Molnar, P., Zhang, P., Xiao, G., Liang, S., Zhang, K., Li, Z., Xu, K., Zhang, L., 2021. Initiation of clockwise rotation and eastward transport of Southeastern Tibet inferred from deflected fault traces and GPS observations. GSA Bull. 134 (5–6), 1129–1142. https://doi.org/10.1130/B36069.1.

Gilfillan, S.M.V., Lollar, B.S., Holland, G., Blagburn, D., Stevens, S., Schoell, M., Cassidy, M., Ding, Z., Zhou, Z., Lacrampe-Couloume, G., Ballentine, C.J., 2009. Solubility trapping in formation water as dominant CO_2 sink in natural gas fields. Nature 458 (7238), 614–618. https://doi.org/10.1038/nature07852.

Gilfillan, S.M.V., Györe, D., Flude, S., Johnson, G., Bond, C.E., Hicks, N., Lister, R., Jones, D.G., Kremer, Y., Haszeldine, R.S., Stuart, F.M., 2019. Noble gases confirm plume-related mantle degassing beneath Southern Africa. Nat. Commun. 10 (1), 5028. https://doi.org/10.1038/s41467-019-12944-6.

Gorczyk, W., Gonzalez, C.M., 2019. CO_2 degassing and melting of metasomatized mantle lithosphere during rifting—Numerical study. Geosci. Front. 10 (4), 1409–1420. https://doi.org/10.1016/j.gsf.2018.11.003.

Graham, D.W., 2002. Noble gas isotope geochemistry of mid-ocean ridge and Ocean Island Basalts: characterization of mantle source reservoirs. Rev. Mineral. Geochem. 47 (1), 247–317. https://doi.org/10.2138/rmg.2002.47.8.

Hao, Y., Kuang, X., Feng, Y., Wang, Y., Zhou, H., Zheng, C., 2023. Discovery and genesis of helium-rich geothermal fluids along the India–Asia continental convergent margin. Geochim. Cosmochim. Acta 360, 175–191. https://doi.org/10.1016/j.gca.2023.09.011.

Guo, Q., Pang, Z., Wang, Y., Tian, J., 2017. Fluid geochemistry and geothermometry applications of the Kangding high-temperature geothermal system in eastern Himalayas. Appl. Geochem. 81, 63–75. https://doi.org/10.1016/j.apgeochem.2017.03.007.

Hanyu, T., Shimizu, K., Ushikubo, T., Kimura, J.-I., Chang, Q., Hamada, M., Ito, M., Iwamori, H., Ishikawa, T., 2019. Tiny droplets of ocean island basalts unveil Earth's deep chlorine cycle. Nat. Commun. 10 (1), 60. https://doi.org/10.1038/s41467-018-07955-8.

Hao, Y., Gong, Q., Kuang, X., Feng, Y., Zhou, H., Zheng, C., 2024. Degassing of mantle-derived helium from hot springs along the India-Asia continental collision settings: origins, migration velocity and flux. Geochem. Geophys. Geosyst. 25 (2), e2023GC011297. https://doi.org/10.1029/2023GC011297.

Hao, Y., Pang, Z., Kong, Y., Tian, J., Wang, Y., Liao, D., Fan, Y., 2020. Chemical and isotopic constraints on the origin of saline waters from a hot spring in the eastern coastal area of China. Hydrogeol. J. 28 (7), 2457–2475. https://doi.org/10.1007/s10040-020-02199-7.

Hao, Y., Wang, Y., Kuang, X., Pang, Z., Li, Y., Feng, Y., Zhou, H., Li, N., Cheng, Y., Li, L., Xing, L., Gong, Q., 2025. Occurrence and enrichment mechanisms of helium in geothermal systems in continental China. Gondwana Res. 141, 289–309. https://doi.org/10.1016/j.gr.2025.02.020.

He, X., Zhao, L.-F., Xie, X.-B., Tian, X., Yao, Z.-X., 2021. Weak crust in southeast Tibetan plateau revealed by Lg-wave attenuation tomography: implications for crustal material escape. J. Geophys. Res. Solid Earth 126 (3), e2020JB020748. https://doi.org/10.1029/2020JB020748.

Hiett, C.D., Newell, D.L., Jessup, M.J., 2021. ^{3}He evidence for fluid transfer and continental hydration above a flat slab. Earth Planet. Sci. Lett. 556, 116722. https://doi.org/10.1016/j.epsl.2020.116722.

Hilton, D.R., Fischer, T.P., Marty, B., 2002. Noble gases and volatile recycling at subduction zones. Rev. Mineral. Geochem. 47 (1), 319–370. https://doi.org/10.2138/rmg.2002.47.9.

Hoefs, J., 2021. Variations of stable isotope ratios in nature. In: Hoefs, J. (Ed.), Stable Isotope Geochemistry. Springer International Publishing, Cham, pp. 267–498. https://doi.org/10.1007/978-3-030-77692-3_3.

Hou, Z., Liu, L., Zhang, H., Xu, B., Wang, Q., Yang, T., Wang, R., Zheng, Y., Li, Y., Gao, L., Yu, N., Wang, X., Miao, Z., Han, S., Lü, Q., 2024. Cenozoic eastward growth of the Tibetan Plateau controlled by tearing of the Indian slab. Nat. Geosci. 17 (3), 255–263. https://doi.org/10.1038/s41561-024-01382-9.

Huang, X., Wang, S., Wang, H., Wang, S., Qi, S., 2024. Hidden magma reservoirs: Insights from helium and carbon isotopic compositions in shallow groundwater beneath the Wudalianchi volcanic field, Northeastern China. Chem. Geol. 666, 122310. https://doi.org/10.1016/j.chemgeo.2024.122310.

Jia, H., 2024. He and CO_2 characteristics around the SE TP. Zenodo. https://doi.org/10.5281/zenodo.13407358.

Kelemen, P.B., Manning, C.E., 2015. Reevaluating carbon fluxes in subduction zones, what goes down, mostly comes up. Proc. Natl. Acad. Sci. 112 (30), E3997–E4006. https://doi.org/10.1073/pnas.1507889112.

Kovács, I.J., Liptai, N., Koptev, A., Cloetingh, S.A.P.L., Lange, T.P., Mațenco, L., Szakács, A., Radulian, M., Berkesi, M., Patkó, L., Molnár, G., Novák, A., Wesztergom, V., Szabó, C., Fancsik, T., 2021. The 'pargasosphere' hypothesis: Looking at global plate tectonics from a new perspective. Global Planet. Change 204, 103547. https://doi.org/10.1016/j.gloplacha.2021.103547.

Lages, J., Rizzo, A.L., Aiuppa, A., Robidoux, P., Aguilar, R., Apaza, F., Masias, P., 2021. Crustal controls on light noble gas isotope variability along the Andean Volcanic Arc. Geochem. Perspect. Lett. 19, 45–49. https://doi.org/10.7185/geochemlet.2134.

Lange, T.P., Palcsu, L., Szakács, A., Kővágó, Á., Gelencsér, O., Gál, Á., Gyila, S., M. Tóth, T., Mațenco, L., Krézsek, C., Lenkey, L., Szabó, C., Kovács, I.J., 2023. The link between lithospheric scale deformations and deep fluid emanations: Inferences from the Southeastern Carpathians, Romania. Evolving Earth, 1: 100013. doi: 10.1016/j.eve.2023.100013.

Lei, J., Zhao, D., 2016. Teleseismic P-wave tomography and mantle dynamics beneath Eastern Tibet. Geochem. Geophys. Geosyst. 17 (5), 1861–1884. https://doi.org/10.1002/2016GC006262.

Li, S., Advokaat, E.L., van Hinsbergen, D.J.J., Koymans, M., Deng, C., Zhu, R., 2017. Paleomagnetic constraints on the Mesozoic-Cenozoic paleolatitudinal and rotational history of Indochina and South China: review and updated kinematic reconstruction. Earth Sci. Rev. 171, 58–77. https://doi.org/10.1016/j.earscirev.2017.05.007.

Li, Y., Chen, Z., Sun, A., Liu, Z., Caracausi, A., Martinelli, G., Lu, C., 2023a. Geochemical features and seismic imaging of the tectonic zone between the Tibetan Plateau and Ordos Block, central northern China. Chem. Geol. 622, 121386. https://doi.org/10.1016/j.chemgeo.2023.121386.

Li, J., Guo, Z., Zhang, M., Zhao, W., Dingwell, D.B., Zheng, G., Sun, Y., Cheng, Z., 2024a. Deep-sourced CO_2 emissions from the Eastern Himalaya Syntaxis and the Tengchong Volcanic Field, southeast Tibet. Chem. Geol. 645, 121888. https://doi.org/10.1016/j.chemgeo.2023.121888.

Li, K., Li, L., Pearson, D.G., Stachel, T., 2019. Diamond isotope compositions indicate altered igneous oceanic crust dominates deep carbon recycling. Earth Planet. Sci. Lett. 516, 190–201. https://doi.org/10.1016/j.epsl.2019.03.041.

Li, K., Li, L., Aubaud, C., Muehlenbachs, K., 2020a. Efficient carbon recycling at the central-northern lesser Antilles arc: implications to deep carbon recycling in global subduction zones. Geophys. Res. Lett. 47 (9), e2020GL086950. https://doi.org/10.1029/2020GL086950.

Li, S., Su, T., Spicer, R.A., Xu, C., Sherlock, S., Halton, A., Hoke, G., Tian, Y., Zhang, S., Zhou, Z., Deng, C., Zhu, R., 2020b. Oligocene deformation of the Chuandian terrane in the SE margin of the Tibetan plateau related to the extrusion of indochina. Tectonics 39 (7), e2019TC005974. https://doi.org/10.1029/2019TC005974.

Li, L., Wang, Y., Gu, H., Lu, L., Li, L., Pang, J., Chen, F., 2022. The genesis mechanism and health risk assessment of high boron water in the Zhaxikang geothermal area, south Tibet. Water. https://doi.org/10.3390/w14203243.

Li, L., Wang, Y., Gu, H., Lu, L., Li, L., Pang, J., Chen, F., 2022. The Genesis Mechanism and Health Risk Assessment of High Boron Water in the Zhaxikang Geothermal Area, South Tibet. Water. https://doi.org/10.3390/w14203243.

Li, Z., Yang, Y., Tong, P., Yang, X., 2023b. Crustal radial anisotropy shear wave velocity of SE Tibet from ambient noise tomography. Tectonophysics 852, 229756. https://doi.org/10.1016/j.tecto.2023.229756.

Li, Z., Zhang, B., Guo, L., Hou, Z., Grasemann, B., Cai, F., Wang, H., 2024b. Slab tear of subducted Indian lithosphere beneath the Eastern Himalayan Syntaxis region. Tectonics 43 (7), e2024TC008248. https://doi.org/10.1029/2024TC008248.

Liu, F., Li, X., Wang, G., Liu, Y., Zhu, H., Kang, J., Huang, F., Sun, W., Xia, X., Zhang, Z., 2017. Marine carbonate component in the mantle beneath the Southeastern Tibetan Plateau: evidence from magnesium and calcium isotopes. J. Geophys. Res. Solid Earth 122 (12), 9729–9744. https://doi.org/10.1002/2017JB014206.

Liu, H., Pei, S., Liu, W., Xue, X., Li, J., Hua, Q., Li, L., 2024. Crustal and upper mantle attenuation structure beneath the Southeastern Tibetan Plateau and its implications on plateau outgrowth. J. Geophys. Res. Solid Earth 129 (2), e2023JB026977. https://doi.org/10.1029/2023JB026977.

Liu, Q.Y., van der Hilst, R.D., Li, Y., Yao, H.J., Chen, J.H., Guo, B., Qi, S.H., Wang, J., Huang, H., Li, S.C., 2014. Eastward expansion of the Tibetan Plateau by crustal flow and strain partitioning across faults. Nat. Geosci. 7 (5), 361–365. https://doi.org/10.1038/ngeo2130.

Liu, Y., Yao, H., Zhang, H., Fang, H., 2021. The Community Velocity Model V.1.0 of Southwest China, Constructed from Joint Body- and Surface-Wave Travel-Time Tomography. Seismol. Res. Lett. 92 (5), 2972–2987. https://doi.org/10.1785/0220200318.

Lopez, T., Fischer, T.P., Plank, T., Malinverno, A., Rizzo, A.L., Rasmussen, D.J., Cottrell, E., Werner, C., Kern, C., Bergfeld, D., Ilanko, T., Andrys, J.L., Kelley, K.A., 2023. Tracking carbon from subduction to outgassing along the Aleutian-Alaska Volcanic Arc. Sci. Adv. 9 (26), eadf3024. https://doi.org/10.1126/sciadv.adf3024.

Lu, Y.-J., Kerrich, R., Cawood, P.A., McCuaig, T.C., Hart, C.J.R., Li, Z.-X., Hou, Z.-Q., Bagas, L., 2012. Zircon SHRIMP U–Pb geochronology of potassic felsic intrusions in western Yunnan, SW China: constraints on the relationship of magmatism to the Jinsha suture. Gondwana Res. 22 (2), 737–747. https://doi.org/10.1016/j.gr.2011.11.016.

Mazza, S.E., Gazel, E., Bizimis, M., Moucha, R., Béguelin, P., Johnson, E.A., McAleer, R. J., Sobolev, A.V., 2019. Sampling the volatile-rich transition zone beneath Bermuda. Nature 569 (7756), 398–403. https://doi.org/10.1038/s41586-019-1183-6.

McCrory, P.A., Constantz, J.E., Hunt, A.G., Blair, J.L., 2016. Helium as a tracer for fluids released from Juan de Fuca lithosphere beneath the Cascadia forearc. Geochem. Geophys. Geosyst. 17 (6), 2434–2449. https://doi.org/10.1002/2015GC006198.

Moreira, M.A., Kurz, M.D., 2013. Noble gases as tracers of mantle processes and magmatic degassing. In: Burnard, P. (Ed.), The Noble Gases as Geochemical Tracers. Springer, Berlin Heidelberg, Berlin, Heidelberg, pp. 371–391. https://doi.org/10.1007/978-3-642-28836-4_12.

Nakao, A., Iwamori, H., Nakakuki, T., 2016. Effects of water transportation on subduction dynamics: Roles of viscosity and density reduction. Earth Planet. Sci. Lett. 454, 178–191. https://doi.org/10.1016/j.epsl.2016.08.016.

Newell, D.L., Benowitz, J.A., Regan, S.P., Hiett, C.D., 2023. Roadblocks and speed limits: Mantle-to-surface volatile flux through the lithospheric-scale Denali fault, Alaska. Geology 51 (6), 576–580. https://doi.org/10.1130/G51068.1.

Omrani, J., Agard, P., Whitechurch, H., Benoit, M., Prouteau, G., Jolivet, L., 2008. Arc-magmatism and subduction history beneath the Zagros Mountains, Iran: A new report of adakites and geodynamic consequences. Lithos 106 (3), 380–398. https://doi.org/10.1016/j.lithos.2008.09.008.

Pinti, D.L., Béland-Otis, C., Tremblay, A., Castro, M.C., Hall, C.M., Marcil, J.-S., Lavoie, J.-Y., Lapointe, R., 2011. Fossil brines preserved in the St-Lawrence Lowlands, Québec, Canada as revealed by their chemistry and noble gas isotopes. Geochim. Cosmochim. Acta 75 (15), 4228–4243. https://doi.org/10.1016/j.gca.2011.05.006.

Plank, T., Manning, C.E., 2019. Subducting carbon. Nature 574 (7778), 343–352. https://doi.org/10.1038/s41586-019-1643-z.

Randazzo, P., Caracausi, A., Aiuppa, A., Cardellini, C., Chiodini, G., D'Alessandro, W., Li Vigni, L., Papic, P., Marinkovic, G., Ionescu, A., 2021. Active degassing of deeply sourced fluids in Central Europe: new evidences from a geochemical study in Serbia. Geochem. Geophys. Geosyst. 22 (11), e2021GC010017. https://doi.org/10.1029/2021GC010017.

Raoof, J., Mukhopadhyay, S., Koulakov, I., Kayal, J.R., 2017. 3-D seismic tomography of the lithosphere and its geodynamic implications beneath the northeast India region. Tectonics 36 (5), 962–980. https://doi.org/10.1002/2016TC004375.

Ray, M.C., Hilton, D.R., Muñoz, J., Fischer, T.P., Shaw, A.M., 2009. The effects of volatile recycling, degassing and crustal contamination on the helium and carbon geochemistry of hydrothermal fluids from the Southern Volcanic Zone of Chile. Chem. Geol. 266 (1), 38–49. https://doi.org/10.1016/j.chemgeo.2008.12.026.

Replumaz, A., Negredo, A.M., Guillot, S., Villaseñor, A., 2010. Multiple episodes of continental subduction during India/Asia convergence: Insight from seismic tomography and tectonic reconstruction. Tectonophysics 483 (1), 125–134. https://doi.org/10.1016/j.tecto.2009.10.007.

Rizzo, A.L., Federico, C., Inguaggiato, S., Sollami, A., Tantillo, M., Vita, F., Bellomo, S., Longo, M., Grassa, F., Liuzzo, M., 2015. The 2014 effusive eruption at Stromboli volcano (Italy): Inferences from soil CO_2 flux and 3He/4He ratio in thermal waters. Geophys. Res. Lett. 42 (7), 2235–2243. https://doi.org/10.1002/2014GL062955.

Royden, L.H., Burchfiel, B.C., van der Hilst, R.D., 2008. The geological evolution of the Tibetan Plateau. Science 321 (5892), 1054–1058. https://doi.org/10.1126/science.1155371.

Sano, Y., Fischer, T.P., 2013. The analysis and interpretation of noble gases in modern hydrothermal systems. In: Burnard, P. (Ed.), The Noble Gases as Geochemical Tracers. Springer Berlin Heidelberg, Berlin, Heidelberg, pp. 249–317. https://doi.org/10.1007/978-3-642-28836-4_10.

Sano, Y., Marty, B., 1995. Origin of carbon in fumarolic gas from island arcs. Chem. Geol. 119 (1), 265–274. https://doi.org/10.1016/0009-2541(94)00097-R.

Shao, W., Liu, Z., Li, Y., Chen, Z., Lu, C., Zhao, C., Wang, Y., Li, Q., Gao, Z., Luo, Y., Ran, H., Fan, S., 2024. Geochemical characteristics of thermal springs and insights into the intersection between the Xiaojiang Fault and the Red River Fault, Southeastern Tibet Plateau. Geochem. Geophys. Geosyst. 25 (3), e2023GC011431. https://doi.org/10.1029/2023GC011431.

Somers, L.D., McKenzie, J.M., 2020. A review of groundwater in high mountain environments. WIREs Water 7 (6), e1475.

Tang, W.-L., Chen, J.-L., Yang, T.-N., Yin, A., Xu, J.-F., Ren, J.-B., 2024. Diverse Late Triassic arc magmatism and porphyry Cu deposits in the southeastern Tibetan Plateau: related to slab tear along a subducting passive margin? Lithos 464–465, 107455. https://doi.org/10.1016/j.lithos.2023.107455.

Tang, X., Wang, Y., Jia, H., Jiang, G., Zuo, Y., Song, R., 2025. Thermal budget of hydrothermal systems for the Xianshuihe fault belt in the SE Tibetan Plateau: Insights to the geothermal accumulation processes. Geothermics 125, 103189. https://doi.org/10.1016/j.geothermics.2024.103189.

Tapponnier, P., Zhiqin, X., Roger, F., Meyer, B., Arnaud, N., Wittlinger, G., Jingsui, Y., 2001. Oblique stepwise rise and growth of the Tibet Plateau. Science 294 (5547), 1671–1677. https://doi.org/10.1126/science.105978.

Thomson, A.R., Walter, M.J., Kohn, S.C., Brooker, R.A., 2016. Slab melting as a barrier to deep carbon subduction. Nature 529 (7584), 76–79. https://doi.org/10.1038/nature16174.

Tian, J., Pang, Z., Wang, Y., Guo, Q., 2019. Fluid geochemistry of the Cuopu high temperature geothermal system in the eastern Himalayan syntaxis with implication on its genesis. Appl. Geochem. 110, 104422. https://doi.org/10.1016/j.apgeochem.2019.104422.

Tian, H.-C., Yang, W., Li, S.-G., Ke, S., Duan, X.-Z., 2018. Low δ^{26}Mg volcanic rocks of Tengchong in Southwestern China: a deep carbon cycle induced by supercritical liquids. Geochim. Cosmochim. Acta 240, 191–219. https://doi.org/10.1016/j.gca.2018.08.032.

Tian, J., Zhou, X., Yan, Y., He, M., Li, J., Dong, J., Liu, F., Ouyang, S., Li, Y., Tian, L., Wang, Y., Huang, T., Pang, Z., 2023. Earthquake-induced impulsive release of water in the fractured aquifer system: Insights from the long-term hydrochemical monitoring of hot springs in the Southeast Tibetan Plateau. Appl. Geochem. 148, 105553. https://doi.org/10.1016/j.apgeochem.2022.105553.

Torgersen, T., 2010. Continental degassing flux of ^{4}He and its variability. Geochem. Geophys. Geosyst. 11 (6). https://doi.org/10.1029/2009GC002930.

Umeda, K., Kusano, T., Asamori, K., McCrank, G.F., 2012. Relationship between ^{3}He/^{4}He ratios and subduction of the Philippine Sea plate beneath southwest Japan. J. Geophys. Res. Solid Earth 117 (B10). https://doi.org/10.1029/2012JB009409.

Van Soest, M.C., Hilton, D.R., Kreulen, R., 1998. Tracing crustal and slab contributions to arc magmatism in the Lesser Antilles island arc using helium and carbon relationships in geothermal fluids. Geochim. Cosmochim. Acta 62 (19), 3323–3335. https://doi.org/10.1016/S0016-7037(98)00241-5.

Wang, Y., Gu, H., Li, D., Lyu, M., Lu, L., Zuo, Y., Song, R., 2021. Hydrochemical characteristics and genesis analysis of geothermal fluid in the Zhaxikang geothermal field in Cuona County, southern Tibet. Environ. Earth Sci. 80 (11), 415. https://doi.org/10.1007/s12665-021-09577-8.

Wang, Z., Kusky, T.M., Capitanio, F.A., 2017. Ancient continental lithosphere dislocated beneath ocean basins along the mid-lithosphere discontinuity: a hypothesis. Geophys. Res. Lett. 44 (18), 9253–9260. https://doi.org/10.1002/2017GL074686.

Wang, Y., Li, L., Wen, H., Hao, Y., 2022. Geochemical evidence for the nonexistence of supercritical geothermal fluids at the Yangbajing geothermal field, southern Tibet. J. Hydrol. 604, 127243. https://doi.org/10.1016/j.jhydrol.2021.127243.

Wang, E., Meng, K., Su, Z., Meng, Q., Chu, J.J., Chen, Z., Wang, G., Shi, X., Liang, X., 2014. Block rotation: tectonic response of the Sichuan basin to the southeastward growth of the Tibetan Plateau along the Xianshuihe-Xiaojiang fault. Tectonics 33 (5), 686–718. https://doi.org/10.1002/2013TC003337.

Wang, W., Qiao, X., Ding, K., 2021. Present-day kinematics in Southeastern Tibet Inferred from GPS measurements. J. Geophys. Res. Solid Earth 126 (1), e2020JB021305. https://doi.org/10.1029/2020JB021305.

Wang, Y., Zhou, X., Tian, J., Zhou, J., He, M., Li, J., Dong, J., Yan, Y., Liu, F., Yao, B., Wang, Y., Zeng, Z., Liu, K., Li, L., Li, Z., Xing, L., 2023. Volatile characteristics and fluxes of He-CO_2 systematics in the southeastern Tibetan Plateau: constraints on regional seismic activities. J. Hydrol. 617, 129042. https://doi.org/10.1016/j.jhydrol.2022.129042.

Wang, Y., Quan, S., Tang, X., Hosono, T., Hao, Y., Tian, J., Pang, Z., 2024. Organic and inorganic carbon sinks reduce long-term deep carbon emissions in the continental collision margin of the Southern Tibetan Plateau: implications for cenozoic climate cooling. J. Geophys. Res. Solid Earth 129 (4), e2024JB028802. https://doi.org/10.1029/2024JB028802.

Wang, Y., Zhou, X., Tian, J., Jia, H., Zhu, X., Li, J., He, M., Zeng, Z., Yan, Y., Yao, B., Wang, Y., Xing, G., Cui, S., Li, L., Li, Z., Cao, C., Xing, L., 2025. Spatiotemporal characteristics of hydrothermal volatiles from the Tengchong volcanic field in the southeastern Tibetan Plateau: a probable constraint on the genesis of intraplate volcanism. J. Volcanol. Geotherm. Res. 457, 108237. https://doi.org/10.1016/j.jvolgeores.2024.108237.

Yao, J., Liu, S., Wei, S., Hubbard, J., Huang, B.-S., Chen, M., Tong, P., 2021. Slab models beneath central Myanmar revealed by a joint inversion of regional and Teleseismic Traveltime Data. J. Geophys. Res. Solid Earth 126 (2), e2020JB020164. https://doi.org/10.1029/2020JB020164.

Zhang, P.-Z., 2013. A review on active tectonics and deep crustal processes of the Western Sichuan region, eastern margin of the Tibetan Plateau. Tectonophysics 584, 7–22. https://doi.org/10.1016/j.tecto.2012.02.021.

Zhang, J., Chen, X., Cai, J., Liu, Z., Dong, Z., Guo, C., Han, B., Jiang, F., Cui, T., 2022. Magnetotelluric evidence for the crustal deformation beneath the region around the Lijiang-Xiaojinhe fault, SE margin of the Tibetan Plateau. J. Asian Earth Sci. 235, 105308. https://doi.org/10.1016/j.jseaes.2022.105308.

Zhang, M., Guo, Z., Sano, Y., Zhang, L., Sun, Y., Cheng, Z., Yang, T.F., 2016. Magma-derived CO_2 emissions in the Tengchong volcanic field, SE Tibet: Implications for deep carbon cycle at intra-continent subduction zone. J. Asian Earth Sci. 127, 76–90. https://doi.org/10.1016/j.jseaes.2016.06.009.

Zhang, M., Guo, Z., Xu, S., Barry, P.H., Sano, Y., Zhang, L., Halldórsson, S.A., Chen, A.-T., Cheng, Z., Liu, C.-Q., Li, S.-L., Lang, Y.-C., Zheng, G., Li, Z., Li, L., Li, Y., 2021. Linking deeply-sourced volatile emissions to plateau growth dynamics in southeastern Tibetan Plateau. Nat. Commun. 12 (1), 4157. https://doi.org/10.1038/s41467-021-24415-y.

Zhang, R., Wu, Y., Gao, Z., Fu, Y.V., Sun, L., Wu, Q., Ding, Z., 2017. Upper mantle discontinuity structure beneath eastern and southeastern Tibet: new constraints on the Tengchong intraplate volcano and signatures of detached lithosphere under the western Yangtze Craton. J. Geophys. Res. Solid Earth 122 (2), 1367–1380. https://doi.org/10.1002/2016JB013551.

Zhang, M., Xu, S., Sano, Y., 2024. Deep carbon recycling viewed from global plate tectonics. Natl. Sci. Rev. 11 (6), nwae089. https://doi.org/10.1093/nsr/nwae089.

Zhao, W., Guo, Z., Zheng, G., Pinti, D.L., Zhang, M., Li, J., Ma, L., 2022. Subducting Indian lithosphere controls the deep carbon emission in Lhasa Terrane, Southern Tibet. J. Geophys. Res. Solid Earth 127 (7), e2022JB024250. https://doi.org/10.1029/2022JB024250.

Zhao, W., Guo, Z., Zhang, M., Sun, Y., Cheng, Z., Li, J., Dingwell, D.B., 2025. Continental subduction and the deep carbon cycle in Northern Tibet. J. Geophys. Res. Solid Earth 130 (1), e2024JB028999. https://doi.org/10.1029/2024JB028999.

Zhou, M.-F., Robinson, P.T., Wang, C.Y., Zhao, J.-H., Yan, D.-P., Gao, J.-F., Malpas, J., 2012. Heterogeneous mantle source and magma differentiation of quaternary arc-like volcanic rocks from Tengchong, SE margin of the Tibetan Plateau. Contrib. Mineral. Petrol. 163 (5), 841–860. https://doi.org/10.1007/s00410-011-0702-8.

Zhou, Y., Xu, B., Hou, Z.Q., Wang, R., Zheng, Y.C., He, W.Y., 2019. Petrogenesis of Cenozoic high–Sr/Y shoshonites and associated mafic microgranular enclaves in an intracontinental setting: Implications for porphyry Cu-Au mineralization in western Yunnan, China. Lithos 324–325, 39–54. https://doi.org/10.1016/j.lithos.2018.10.031.

Zhu, R.-Z., Słaby, E., Lai, S.-C., Chen, L.-H., Qin, J., Zhang, C., Zhao, S., Zhang, F., Liu, W.-H., Fowler, M., 2021. High-K calc-alkaline to shoshonitic intrusions in SE Tibet: implications for metasomatized lithospheric mantle beneath an active

continental margin. Contrib. Mineral. Petrol. 176 (10), 85. https://doi.org/10.1007/s00410-021-01843-z.

Zhu, H., Tian, Y., Zhao, D., Li, H., Liu, C., 2019. Seismic structure of the Changbai intraplate volcano in NE China from joint inversion of ambient noise and receiver functions. J. Geophys. Res. Solid Earth 124 (5), 4984–5002. https://doi.org/10.1029/2018JB016600.

Zou, H., Ma, M., Fan, Q., Xu, B., Li, S.-Q., Zhao, Y., King, D.T., 2017. Genesis and open-system evolution of Quaternary magmas beneath southeastern margin of Tibet: constraints from Sr-Nd-Pb-Hf isotope systematics. Lithos 272–273, 278–290. https://doi.org/10.1016/j.lithos.2016.12.012.

Zummo, F., Agosta, F., Álvarez-Valero, A.M., Billi, A., Buttitta, D., Caracausi, A., Carnevale, G., Marchesini, B., Paternoster, M., 2024. Tracing a mantle component in both paleo and modern fluids along seismogenic faults of Southern Italy. Geochem. Geophys. Geosyst. 25 (11), e2024GC011816. https://doi.org/10.1029/2024GC011816.

Zuo, Y., Sun, Y., Zhang, L., Zhang, C., Wang, Y., Jiang, G., Wang, X., Zhang, T., Cui, L., 2024. Geothermal resource evaluation in the Sichuan Basin and suggestions for the development and utilization of abandoned oil and gas wells. Renew. Energy 225, 120362. https://doi.org/10.1016/j.renene.2024.120362.